

Simulation of Shaped Comb Actuator for Controlled Displacement Applications

by

Isabelle Pacheco Fernandes Harouche

A thesis
submitted to the Faculty of Graduate Studies
in partial fulfilment of the requirements for the degree of

MASTER OF SCIENCE

Department of Electrical and Computer Engineering
University of Manitoba
Winnipeg, Manitoba

© Isabelle P. F. Harouche, November 2004.

THE UNIVERSITY OF MANITOBA
FACULTY OF GRADUATE STUDIES

COPYRIGHT PERMISSION

**Simulation of Shaped Comb Actuator for
Controlled Displacement Applications**

BY

Isabelle Pacheco Fernandes Harouche

**A Thesis/Practicum submitted to the Faculty of Graduate Studies of The University of
Manitoba in partial fulfillment of the requirement of the degree
Master Of Science**

Isabelle P.F. Harouche © 2005

Permission has been granted to the Library of the University of Manitoba to lend or sell copies of this thesis/practicum, to the National Library of Canada to microfilm this thesis and to lend or sell copies of the film, and to University Microfilms Inc. to publish an abstract of this thesis/practicum.

This reproduction or copy of this thesis has been made available by authority of the copyright owner solely for the purpose of private study and research, and may only be reproduced and copied as permitted by copyright laws or with express written authorization from the copyright owner.

Abstract

A shaped, interdigitated comb drive is introduced as a viable actuator for microtweezers. The device offers prescribed output force for known actuation voltage steps. As a result, controllable displacement is achieved. Partial device closure and engagement force control are possible through the achieved step-movement. The displacement is linked to the change in capacitance due to the varying engaging geometry of the device.

Finite element analysis is used to simulate the electrostatic actuated, shaped comb drives operating under DC conditions (zero actuating frequency). A parametric multiphysics model is developed using the Arbitrary Lagrangian-Eulerian (ALE) formulation. Results show the coupled interaction between the electrostatic and mechanical domains of the transducer. The analysis is based on the evolution of electrostatic force versus comb finger engagement. The relationship between incremental lateral displacement and actuation voltage illustrates the potential for stepped movement for a shaped comb drive. Additionally, through numerical simulations, this project determines an ideal design for a DC-actuated comb drive, which has controllable force output and stable engaging movement.

Acknowledgements

I would like to acknowledge the help and suggestions of my thesis advisor, Dr. Cyrus Shafai, whose stimulating input made this thesis possible. Most importantly, I am most thankful for his endless and unconditional support during my engineering graduate school years.

I would also like to express my gratitude to the following people:

- The whole team of professors and graduate students at the MEMS/SPM Lab, specifically Behraad Bahreyni and Dwayne D. Chrusch for their valuable suggestions throughout this thesis.
- Mr. Linus Andersson from COMSOL AB for his precious technical help,
- Dr. Richard Gordon and the Health Sciences Centre Foundation for the partial financial support of this project, and
- Shawn Silverman, for his friendship, presence and culinary skills. ☺

Lastly, I would like to thank my parents, Edna and Paulo, for their support. Despite the distance, they have been always by my side.

Table of Contents

ABSTRACT	ii
ACKNOWLEDGEMENTS	iii
TABLE OF CONTENTS	iv
LIST OF FIGURES	vi
LIST OF TABLES	ix
NOMENCLATURE.....	x
CHAPTER 1 INTRODUCTION	1
1.1 RESEARCH GOALS	2
1.2 DESIGN CONCEPT	3
1.3 REPORT ORGANIZATION.....	4
CHAPTER 2 BACKGROUND ON COMB DRIVES AND MICROTWEEZERS.....	5
PART I – COMB DRIVES.....	5
2.1 ELECTROPHYSICS OF COMB ACTUATORS.....	7
2.2 ASYMMETRIC COMB DRIVES	13
2.3 ARBITRARILY-SHAPED COMB DRIVES	13
2.4 SAW-TOOTH COMB DRIVE	16
PART II – MICROTWEEZERS ACTUATION SYSTEM.....	18
2.5 THERMAL ACTUATION	18
2.6 ELECTROSTATIC ACTUATION.....	20
CHAPTER 3 BACKGROUND ON THE NUMERICAL ANALYSIS OF COMB DRIVE ...	22
3.1 GENERAL DESCRIPTION OF THE PROBLEM	22
3.1.1 <i>Electrostatic Analysis</i>	22
3.1.2 <i>Mechanical Analysis</i>	25
3.2 THE ARBITRARY LAGRANGIAN-EULERIAN FORMULATION.....	29
3.2.1 <i>Introduction</i>	29
3.2.2 <i>The ALE and the Comb Drive Simulation</i>	31

3.2.3	<i>Problem Definition</i>	34
3.3	CONCLUSION	37
CHAPTER 4	FABRICATION AND INITIAL TESTING	39
4.1	PREAMBLE	39
4.2	DESIGN CONSIDERATIONS	40
4.3	FABRICATION PROCEDURES	41
4.4	DESIGN RESULTS	43
4.5	TESTING	45
4.6	CONCLUSION	47
CHAPTER 5	DESIGN SIMULATIONS AND NUMERICAL SOLUTIONS	48
5.1	PREAMBLE	48
5.2	MESH GENERATION	49
	PART I – INDEPENDENT 3D SIMULATION	52
5.3	ELECTROSTATIC SIMULATION	53
5.4	PLANE STRESS SIMULATION	60
5.5	STEPPED MOVEMENT	62
	PART II - ELECTROMECHANICAL MULTIPHYSICS SOLUTION	65
5.6	THE COMB DRIVE ANALYSIS WITH ALE	66
5.7	FORMULATIONS AND SIMULATION SET-UP	67
5.8	RESULTS FROM THE PARAMETRIC ANALYSIS	73
5.8.1	<i>Discussion on Proposed Shapes</i>	77
5.9	CONCLUSION	84
CHAPTER 6	THESIS SUMMARY AND FUTURE CONSIDERATIONS	85
6.1	PREAMBLE	85
6.2	SUMMARY OF INVESTIGATIONS	85
6.3	PROPOSED DESIGN RULE	87
6.4	FUTURE CONSIDERATIONS	88
	REFERENCES	90
APPENDIX I	THE PRINCIPLE OF VIRTUAL WORK	94
APPENDIX II	THEORETICAL PRINCIPLES OF FEM	97
APPENDIX III	Femlab CODE	105

List of Figures

Figure 1.1. Basic design of a comb drive.	1
Figure 1.2. Ideal design of the integrated microtweezers with a shaped comb drive actuator.....	3
Figure 2.1. Detailed schematic description of a comb drive. The grey structures represent free-standing, movable parts; black represents anchored parts. White cross-boxes represent the anchor attached to the substrate.	6
Figure 2.2. Schematics of field lines distribution: description of local forces, where d is the fixed distance between comb fingers and ς is the side-wall surface.	8
Figure 2.3. Schematics describing the field lines in a semi-engaged rectangular comb-drive. Displacement occurs in the Y-direction. Red represents the fixed fingers and blue stands for the movable finger.	10
Figure 2.4. Asymmetric unit comb drive.....	13
Figure 2.5. Schematics of two arbitrarily-shaped comb fingers. The out-of-plane thickness is defined as t and ς is the finger side-wall surface corresponding to the engaged distance Y_0	14
Figure 2.6. Schematics describing the engagement of one rectangular-shaped finger with respect to a fixed arbitrarily-shaped finger.....	16
Figure 2.7. Sawtooth comb design and its characteristic force versus engagement plot from [6].....	17
Figure 2.8. Thermally actuated microtweezers as described by Keller and Howe [23]. This picture has been downloaded from the author's website (www.memspi.com).	19
Figure 2.9. Drive mechanism for one of the two microtweezers arms for the device developed in [14]. Point a is closer to the cantilever pivot point and the total displacement at this point is less than that at b	20
Figure 3.1. Schematic description of the spring beam boundary conditions.	28
Figure 3.2. This is an illustrative demonstration of the interaction between the electrostatic problem and the ALE grid displacement.	32
Figure 3.3. Flowchart describing the ALE procedure.....	38
Figure 4.1. View of the X-Y plane of the three simulated comb shaped. From top to bottom: rectangular, sawtooth, and jagged-edge.....	39
Figure 4.2. Schematic description of the fabricated spring. The shuttle is the mounting structure where the comb drive is attached.....	40

Figure 4.3. Jagged-edge shape comb drive viewed through a 50X enlargement objective. The detail shows the 100X enlargement of a unit comb finger.	43
Figure 4.4. Sawtooth shape comb drive viewed through a 50X enlargement objective. The detail shows the 100X enlargement of a unit comb finger.	44
Figure 4.5. Rectangular shape comb drive viewed through a 50X enlargement objective. The detail shows the 100X enlargement of a unit comb finger.	44
Figure 4.6. Schematic description of the testing environment. The shuttle shared the same ground as one of the fixed fingers.	46
Figure 5.1. Mesh density analysis. The arrow points to the “coarser” mesh solution.	50
Figure 5.2. Example of a quality histogram for the Femlab automatic <i>coarser</i> mesh analysis with quadratic element. This case study is based on a 2D rectangular comb drive.	51
Figure 5.3. Independent electrostatic (left column) and mechanical analysis (right column).	52
Figure 5.4. Potential field distribution results for a 26- μm engagement of three different comb finger shapes. The dimensions of the total integration area are shown in (c). Excerpts (d) depict the details of field distribution around each finger.	54
Figure 5.5. The bold shapes represent total capacitance values recovered from the 3D simulations. The hollow shapes represent total capacitance values from the 2D simulations.	56
Figure 5.6. Streamlines illustrating the electric field distribution (E). The surrounding volume and device edges follow the electric potential scale 0-100V.	56
Figure 5.7. Comparison between 2- and 3-dimensional integrations of capacitances. The x - coordinates give the distance between the device boundaries and the surrounding volume boundaries (as described in Figure 5.4).	57
Figure 5.8. These curves represent total capacitance in the jagged-edge model for three different simulation conditions: 3D with Si substrate, 3D without substrate, and 2D.	59
Figure 5.9. Differential capacitance with respect to finger displacement.	59
Figure 5.10. Spring design. The spring beam length was simulated for three different lengths:	60
Figure 5.11. Spring displacement due to applied force. F_{mech} is equal in magnitude and direction to F_{es} for a given step movement.	61
Figure 5.12. Stiffness plot for all three modelled springs with different nominal lengths. The arrows point to each spring constant value.	62
Figure 5.13. Required force for prescribed engagement.	63
Figure 5.14. Higher actuation voltages are required for implementing the 140- μm spring.	64
Figure 5.15. Constraints defined in all three multiphysics modes.	70
Figure 5.16. Artificial montage depicting the evolution of field lines with increasing voltage.	74

Figure 5.17. Force and force gradient with respect to finger engagement from rest position. Both plots show the force acting on the set of movable (a) jagged-edge fingers and, (b) rectangular fingers.....	75
Figure 5.18. FEM solution for the rectangular comb drive. This plot depicts the 200V input parameter. ...	76
Figure 5.19. Schematic description of: (A) MUMPs design; (B-E) newly proposed jagged-edge finger shapes; (F) rectangular comb finger.....	77
Figure 5.20. Comb displacement with respect to the actuation voltage V_0 . (a) Results from the 8:2 μ m-gap; (b) results from the 4:1 μ m-gap. The reader should note the difference in scales in the differential displacement axes.	78
Figure 5.21. Force and force gradient results for both the 4:1 μ m-gap and 8:2 μ m-gap designs.	79
Figure 5.22. Simulated differential displacement with respect to actuation voltage for both symmetric and asymmetric 7:1 designs.	80
Figure 5.23. Comparison of differential displacements of all geometries investigated.	82
Figure 5.24. Analysis of the 7:1 symmetric design (shape D)	83
Figure 5.25. Analysis of the 7:1 asymmetric design (shape E).....	83

List of Tables

Table 2-1. Variables of interest in a comb drive design and operation. The reader should refer to Figure 2.1 for better understanding of each one of these variables.....	12
Table 4-1. MUMPs process flow. The steps described here are those relevant to the comb drive fabrication. All schematics are from [7].	42
Table 5-1. Qualitative description of the user-software interaction.....	71

Nomenclature

This section introduces the nomenclature used in all mathematical expressions and schematics presented in this thesis. Extensive descriptions are given through this paper but, whenever necessary, the reader is encouraged to use this list as a resource. Attention must be given to differences in italicized, bolded and Greek letters.

NOMENCLATURE - ROMAN LETTERS -	UNITS AND CONSTANT VALUES	DESCRIPTION
C	[F]	Capacitance
d	[m]	Gap distance between comb fingers
D	[C/m ²]	Electric flux density.
E	[V/m]	Electrostatic field intensity
E	[Pa]	Young's Modulus
F_{es}	[N]	Electrostatic force
H	[A/m]	Magnetic field intensity
J	[C/s/m ²]	Current density.
k	[N/m]	Spring constant.
t	[m]	Comb finger thickness or <i>structural layer</i> thickness.
V_0	[V]	Actuation potential bias
W_e	[J]	Electrostatic energy
X		Cartesian axis or arbitrary distance in the X-axis
Y		Cartesian axis or arbitrary distance in the Y-axis
Z		Cartesian axis or arbitrary distance in the Z-axis
NOMENCLATURE - GREEK LETTERS -		DESCRIPTION
ϵ_0	8.854×10^{-12} [F/m]	Constant permittivity of free space
ϵ	<i>dimensionless</i>	Strain normal to the X-axis.
ϵ_{YY}	<i>dimensionless</i>	Strain normal to the Y-axis
ϵ_{XY}	<i>dimensionless</i>	Shear strain.
μ_0	$4\pi \times 10^{-7}$ [N/A ²]	Magnetic permeability of free space
ν	<i>dimensionless</i>	Poisson's ratio.
ρ	[C]	Volume charge
σ	[N/m ²]	Mechanical stress normal to the X-axis.
σ_{YY}	[N/m ²]	Mechanical stress normal to the Y-axis.
σ_{XY}	[N/m ²]	Shear stress
S	[m ²]	Comb finger overlapping sidewall area. This corresponds to the <i>engaged</i> distance.

Chapter 1 Introduction

Capacitance-based sensors and actuators have been extensively used in microelectromechanical systems (MEMS) [1],[2]. Among different devices, the most commonly used and analysed is the *comb drive* [1],[4], seen in Figure 1.1. The MEMS comb drive is a laterally driven mechanical actuator activated by electrostatic interaction. The basic design of a comb drive relies on the theory of parallel-plate capacitors, which in turn is a function of the plates' area and shape. In the case of a comb drive, the parallel plates are an array of interdigitated fingers, which are generally rectangular. Different finger shapes and their electrostatic characteristics are discussed in this report.

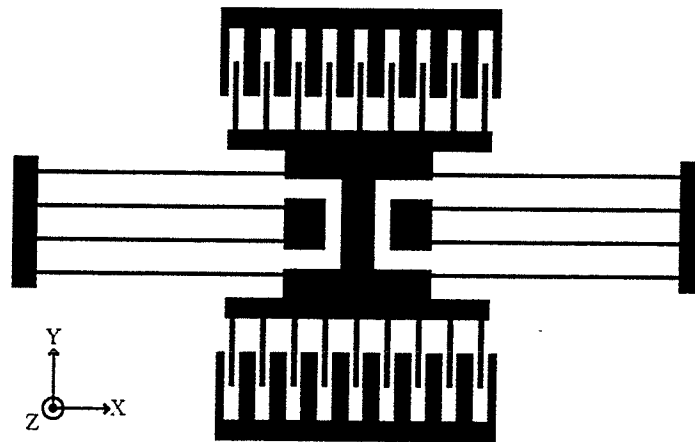


Figure 1.1. Basic design of a comb drive.

A typical rectangular-shaped comb drive design requires simple fabrication steps (usually only one structural layer) and is characterized by low power consumption [5]. Disadvantages associated with the usual rectangular design are briefly summarized as

nonlinear force-to-voltage relationship and lower output power and efficiency than that which is predicted by models [6]. Comb drives have been used as actuators for several different applications, including but not restricted to micro-motors, conveyors, sensing devices and microgrippers devices.

1.1 Research Goals

The present work introduces a novel step-and-lock mechanism based on the comb drive design. The main use for such device would be as a microtweezers actuator for application in areas such as biological sample handling, MEMS assembly processes and other activities where precision micromanipulation and displacement-controlled interaction are required.

Throughout this text the original rectangular comb drive is presented and its operational characteristics are discussed. This device was originally designed for high frequency operation as resonators. Later, shaped comb drives were introduced [6] as a means to stiffen and weaken resonator springs and hence offer more controllability over the device operation. Using sawtooth- and polynomial-shaped comb teeth, *tunable resonators* were proposed as a means to achieve linear force-deflection profiles

1.2 Design Concept

This project introduces an adaptation to the shaped comb drives analyzed in [6], in that the force-displacement is not linear, but it is also not constant, as in the case of rectangular comb drives. Instead, a stepped force response versus displacement is made possible by using jagged-edge comb teeth, as illustrated in Figure 1.2. The same figure offers a conceptual idea of a possible final design for a displacement controllable microtweezers. This report pertains to the actuator design. The gripping pads and final microtweezers testing are left for future work. The proposed move-and-lock mechanism is based on the change in the lateral distance between the fixed and movable comb fingers with respect to engagement, which in turn is a function of the actuation voltage. The geometry simulated in this thesis corresponded to a set of ten fixed and nine movable fingers.

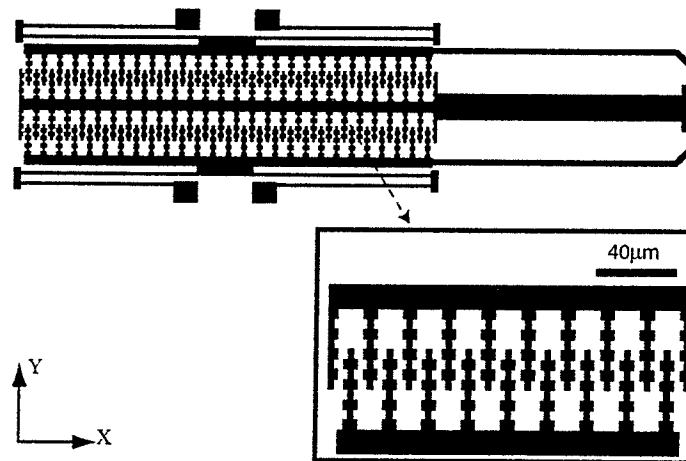


Figure 1.2. Ideal design of the integrated microtweezers with a shaped comb drive actuator.

1.3 Report Organization

This report describes comb drives from the perspective of electrostatic interaction model, shape design, fabrication, and applications. Chapter 2 offers an overview of comb drive design and research so far. The device is introduced as an actuator for the purpose of applications where fine displacement control is needed. Next, micro-gripping devices are introduced and shaped comb drives are discussed in the context of a microtweezers actuation system.

Chapter 3 engages in a thorough description of the numerical methods used for the device simulation. A description of the problem, both from the electrostatic and mechanical points of views is given. The initial device fabrication and testing procedures are discussed in Chapter 4. In that section, a brief description of the device fabrication through the *multi-users MEMS Process* (MUMPs) [7] is given. Since the device was fabricated by a third-party, the focus of the chapter is to offer enough supporting information for the structure simulation discussion. Limitations in the fabrication requirements led to non-ideal testing conditions.

In Chapter 4, the reader will find the numerical simulations performed with the finite element method. These are used to discuss suggested improvements in the conceptual design. This discussion leads into the conclusions achieved in this project and future work ideas are suggested.

Chapter 2 Background on Comb Drives and Microtweezers

Part I – Comb Drives

Comb drives are laterally driven, electrostatic actuators widely used in the MEMS industry. The device was first introduced in 1989 [3], [4] and since then it has been applied in a variety of applications that require electrostatic sensing [1], [8] and electromechanical driving [2].

The most basic comb drive design can be seen in Figure 2.1, where the grey colour represents free-standing, movable parts, whereas black depicts the anchored parts. The comb drive is a polysilicon microstructure parallel to the substrate plane. It has two pairs of double folded cantilever springs attached to a shuttle, which in turn carries the movable electrostatic fingers. In general, parallel plate electrodes display low hysteresis and no magnetic fluxes, producing large output forces [5].

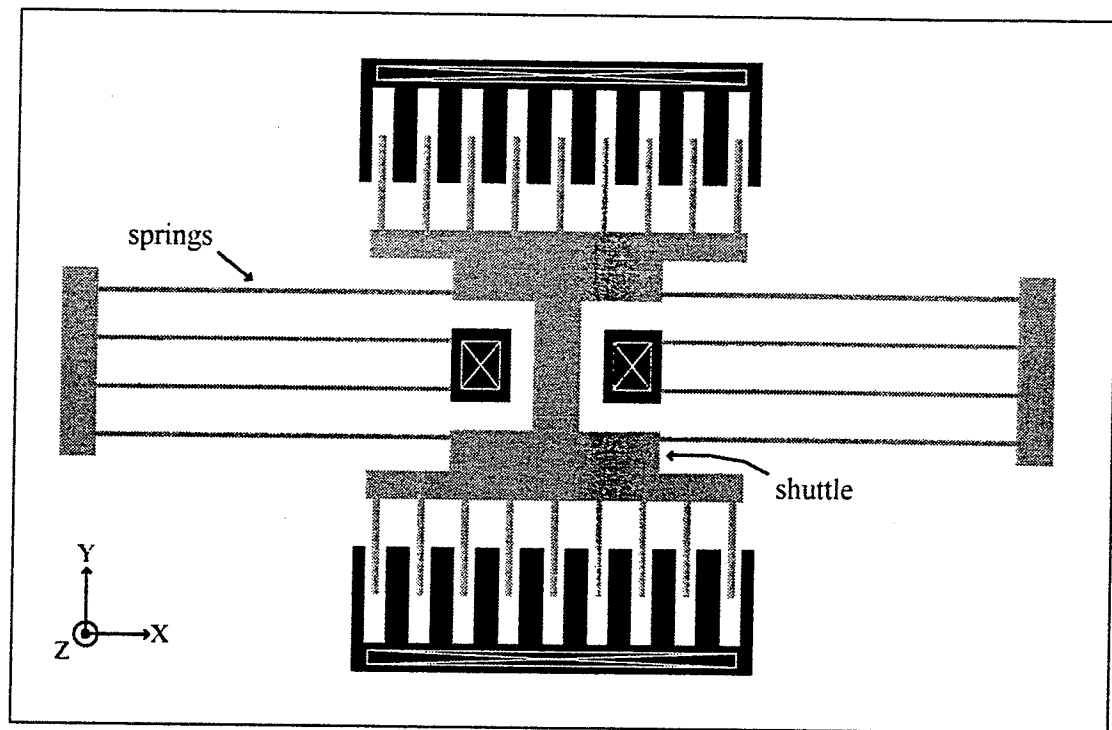


Figure 2.1. Detailed schematic description of a comb drive. The grey structures represent free-standing, movable parts; black represents anchored parts. White cross-boxes represent the anchor attached to the substrate.

Several authors have modelled and simulated comb drives under different conditions. Comb drives can be simulated from the perspective of one single set of engaging fingers, henceforth referred to as *unit comb drive*. Simulation results from a unit comb drive render information regarding differential capacitance with respect to displacement and electrostatic forces [4], [6]. Conversely, models can demonstrate the total capacitance of a set of fingers in free space or take into account the grounded plane below the structure, which yields a more accurate understanding of fringing fields [9].

The following section will present and discuss some of the previous work done in the fields of design and simulation of comb drives. Double-folded cantilever springs will be described to some extent, since the mechanical restoring force is an integral part of the comb drive simulation. Ultimately this review will lead into a discussion of the use of comb drives as an actuator mechanism for microtweezers.

2.1 Electrophysics of Comb Actuators

In what follows, a few basic electrostatic principles relevant to the comb drive operation are presented. A detailed description of the electrostatic principles of comb drives can be found elsewhere [5].

The forces interacting in a comb drive can be described by two components: *local* and *global*. Local forces are associated with potential sheets limited to the cross-sections of any given comb finger. Global forces are corrections related to the electric fields resulting from equipotential sheets, which represent both the engaged and unengaged comb finger regions. Figure 2.2 represents a schematic description of local forces, which are defined by electric field lines in the X-Z plane, whereas global forces are defined in the Y-Z plane; both cases are described in a confined in a symmetric and homogeneous surrounding area filled with air.

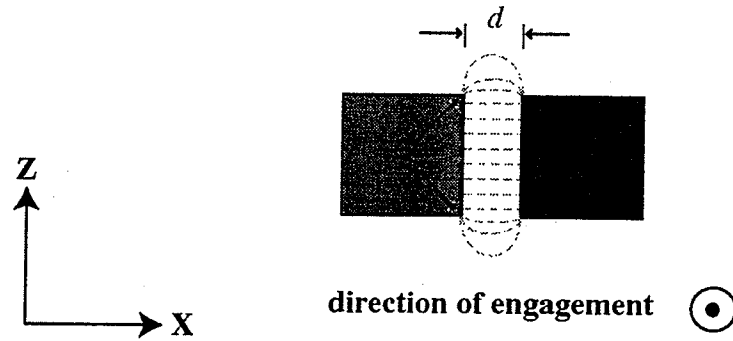


Figure 2.2. Schematics of field lines distribution: description of local forces, where d is the fixed distance between comb fingers and ζ is the side-wall surface.

Let *large engagement* be defined as any engagement distance $Y_0 \gg d$, where d is the constant gap distance between fingers. In a three-dimensional structure where the fingers are initially largely engaged, fringing fields exist according to the principle of parallel plate capacitors. If the distance d is considerably smaller than the length and thickness of the plates, fringing fields can be neglected, since most field lines are restricted to the finger cross-sections region (Figure 2.2). Additionally, the fringing fields at the end of the fingers do not change significantly with further engagement. It follows that the capacitance between any two plates is a function of the total engaged overlapping surface area of the plates ζ and the gap distance d , as per equation (2-1).

$$C = \epsilon_0 \frac{\zeta}{d} \quad (2-1)$$

Equation (2-1) only accounts for the field lines confined between the capacitor plates. This is a reasonable approximation in the cases where fringing fields are negligible and the surrounding dielectric is symmetric about the structure. However, if

the gap distance d is larger than one of the dimensions of the plate, the previous assumption is not correct and fringing fields will interfere in the total capacitance calculation. In this case, the capacitance is retrieved from equation (2-2):

$$C_{\text{TOT}} = \frac{2}{V_0^2} \iiint_{XYZ} W_e dXdYdZ \quad (2-2)$$

The electrostatic field energy W_e relative to the same volume of integration as in (2-2) is:

$$W_e = -\frac{1}{2} \epsilon_0 \iiint_{XYZ} |\mathbf{E}|^2 dXdYdZ \quad (2-3)$$

It follows that the attractive electrostatic force F_{es} in the Y-direction is a function of capacitance and inversely proportional to the gap between fingers, as equation (2-4).

$$F_{es} = \frac{\partial W_e}{\partial Y} = \frac{1}{2} \frac{\partial C}{\partial Y} V_0^2 \quad (2-4)$$

The force F_{es} is generated by the fringing fields connecting the sidewalls of the movable finger to those in the fixed finger. Thus, the effective attractive force is caused by the Y-component of the potential lines connecting the movable finger and the fixed finger (Figure 2.3). Due to symmetry, all other X-component force vectors are cancelled with its respective opposite.

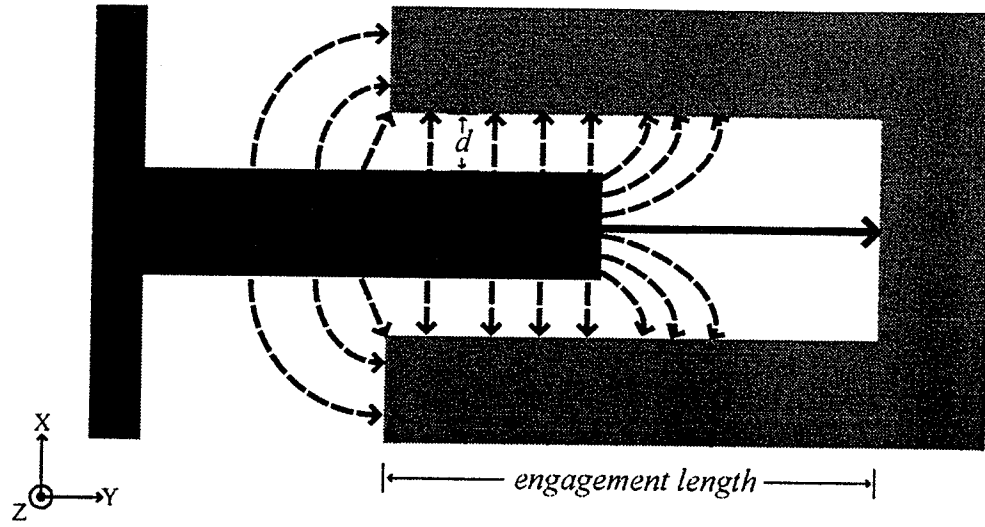


Figure 2.3. Schematics describing the field lines in a semi-engaged rectangular comb-drive. Displacement occurs in the Y-direction. Red represents the fixed fingers and blue stands for the movable finger.

Since the d gap between fingers is constant, $\partial C/\partial Y$ is largely the same for any displacement Y_0 less than the total finger engagement length [5]. Therefore, under the assumption of initial large engagement, the electrostatic engaging force F_{es} is constant at any displacement point. Yeh *et al.* [11] stated a closed form analytical solution, which defines the minimum initial engagement that assures constant output force. This description is valid for the field lines confined in the overlapping region and it agrees with the analytical model given by the author in [4]. However, a more realistic model would account for a ground plane below the comb drive device. In this case, the sole use of equations (2-3) and (2-4) to describe the effective sheet potentials would be prone to errors. The authors in [10] warned that calculations of both the electrostatic force F_{es} and the potential energy W_e must account for the non-engaged area between the fixed finger

Chapter 2 Background on Comb Drives and Microtweezers

as well. Therefore, the proper description of F_{es} should follow equation (2-5a-c). The superscripts (f) and $(f+m)$ represent the *fixed* and the *fixed and movable* overlapping sidewall surfaces respectively. Despite the more accurate analytical description of the problem, the authors in [11] agreed that due to the complexity in describing transition regions, a numerical solution would offer more insight.

$$\left\{ \begin{array}{l} F_{es} = F_{es}^{(f+m)} + F_{es}^{(f)} \quad (a) \\ F_{es}^{(f+m)} = \frac{1}{2} \frac{\partial W_e^{(f+m)}}{\partial Y} \quad (b) \\ F_{es}^{(f)} = \frac{1}{2} \frac{\partial W_e^{(f)}}{\partial Y} \quad (c) \end{array} \right. \quad (2-5)$$

It is important to consider that the total comb finger displacement can vary on a number of extra coexisting factors; namely, the number of fingers, dimensions of each finger, voltage applied, dimensions of spring structures and materials used. Table 2-1 describes the role of each variable in a comb drive design and analyses how they influence on the device operation. Detailed explanations regarding each of the variables are found throughout this report.

Chapter 2 Background on Comb Drives and Microtweezers

Table 2-1. Variables of interest in a comb drive design and operation. The reader should refer to Figure 2.1 for better understanding of each one of these variables.

Variable	Description
Spring Length	Longer springs reduce the equivalent spring constant.
Spring Width	Lower width reduces the equivalent spring constant. A change from 1- to 2- μm in the spring width will increase the total possible displacement by a factor of 8.
Number of Fingers	Total number of fingers present in the device, i.e., both grounded and charged fingers. More fingers will increase total electrostatic force.
Comb Gap Distance	Gap distance between a charged and grounded finger. Smaller spacing increases the total electrostatic force.
Comb Thickness	Thickness of the comb fingers (Z-axis) as well as the structure attached to the comb fingers. Greater thickness (change in area) increases the total electrostatic force.
Spring Thickness	Typically the same as <i>comb thickness</i> . Thinner spring thickness decreases the equivalent spring constant.
Comb Finger Overlap	Initial finger overlap before any voltage is applied. It has a large impact on the stability and useful range of the device (implications in preventing short between movable and fixed fingers).
Voltage Bias	DC Voltage applied to one comb structure (either movable or fixed set of fingers). The opposing comb structure is set to $V=0$ (ground potential).
Structure Material	It defines the modulus of elasticity and consequently the calculations of moment of inertia. The comb drives presented in this report are all made of Si (poly- or single crystal)

So far the analytical description of comb drives has been based on the generic rectangular-shaped finger. It has been established that the leading variable in defining the electrostatic properties of the comb drive is capacitance. Equation (2-1) relates capacitance with the geometry of the plates. Thus, it is a trivial assumption that change in geometry will cause a response change in capacitance, which in turn will affect the distribution of equipotential lines and electrostatic force vectors. Such variations in geometry may be represented by an actual change in the capacitive plate shape, which would affect both variables ζ and d in equation (2-1). The following sections will discuss previously published research work dealing with varying the shapes of comb drives.

2.2 Asymmetric Comb Drives

Yeh *et al.* [11] explored the effects of an asymmetric comb drive (Figure 2.4) and developed an analytical solution for this problem. Asymmetric comb drives deliver large out-of-plane motion. This device has thin movable fingers which, when in rest, are placed higher than the thicker, substrate-attached, fixed fingers. The actuation process occurs when the thin fingers are pulled down towards the substrate due to a difference in potential among the fingers. Fringing fields are the essential component of the electrostatic force.

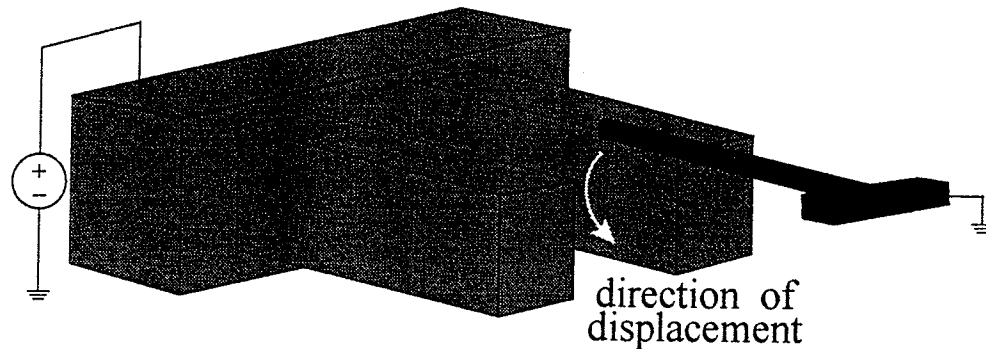


Figure 2.4. Asymmetric unit comb drive.

2.3 Arbitrarily-Shaped Comb Drives

Different output force profiles as a function of finger displacement are achieved by customizing the comb drive finger shape. The authors in [12] used numerical analysis to optimize the comb finger shape according to the desired force response. The analysis encompassed both the comb drive and the suspension spring. The restoring spring force

was found to be non-linear for large displacements, hence the need to increase the force output with engagement. The driving force acting on the moving fingers along the direction of displacement Y is:

$$F_{es} = \int_{\zeta} F_{es_Y} d\zeta \quad (2-6)$$

where F_{es_Y} is the component of the electrostatic force in the Y direction computed on the surface ζ . Figure 2.5 shows that ζ corresponds to the engaged distance Y_0 of each comb finger (conductor plate).

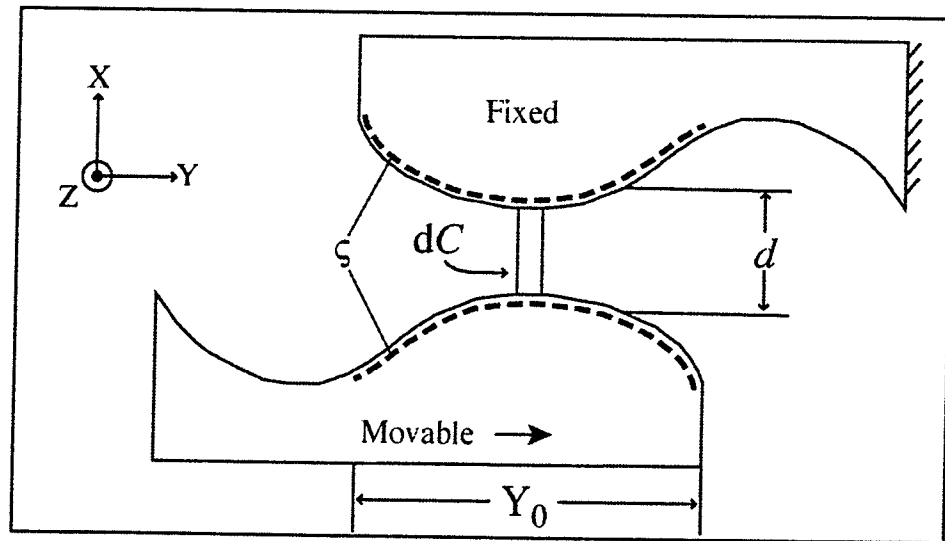


Figure 2.5. Schematics of two arbitrarily-shaped comb fingers. The out-of-plane thickness is defined as t and ζ is the finger side-wall surface corresponding to the engaged distance Y_0 .

It follows that F_{es_Y} is defined by equation (2-7):

$$F_{es_Y}(\zeta) = \epsilon t \frac{V^2}{d(\zeta)} \quad (2-7)$$

where t is the out-of-plane finger thickness and d is the gap between movable and fixed

finger at any point in the engagement. Therefore, with a non-rectangular shape, the gap d will undoubtedly vary with the movable displacement. Previous reports [12], [13] depicted several force-versus-displacement profiles for a variety of shaped of fixed fingers. Driving forces were tailored to linear, quadratic and cubic responses.

Jensen *et al.* [6] discussed the concept of *customized force-displacement* response as well as developed a generic model for any shape of finger. The final goal of the research was to achieve tunable resonators, which allow both up and down shifts of the resonant frequency. The model was tested for seven different finger shapes, each representing a single set of capacitors. Neither the analytical model nor the boundary element method simulations described by these authors accounted for the restoring mechanical spring force. The analytical model assumed a unit comb drive with one rectangular movable finger and one arbitrarily-shaped fixed finger (Figure 2.6). The shape of the side wall of the movable rectangular finger is a constant k , whereas the fixed finger is described by a function $g(Y)$. It follows that the gap between the fingers is $h(Y) = g(Y) - k$ and the total capacitance is (ignoring fringing) computed as:

$$C = 2\epsilon_0 t \int_0^{Y_1} \frac{dY}{h(Y)} \quad (2-8)$$

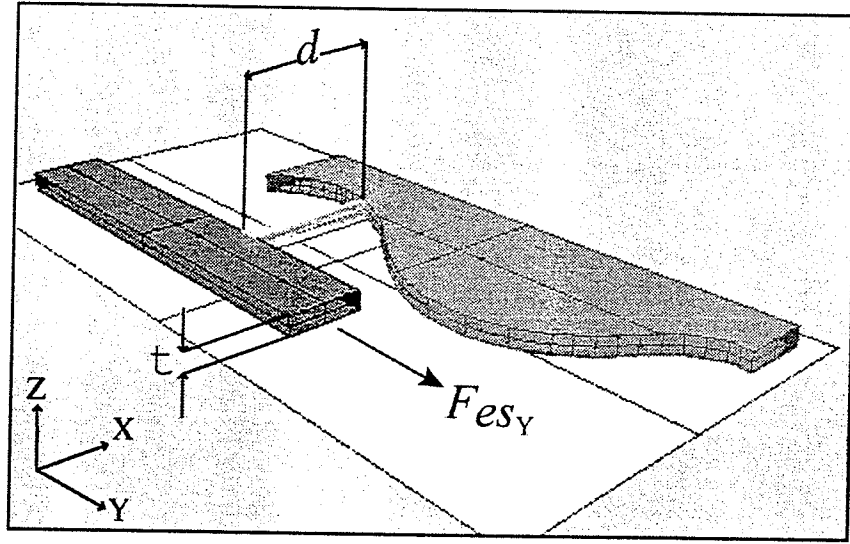


Figure 2.6. Schematics describing the engagement of one rectangular-shaped finger with respect to a fixed arbitrarily-shaped finger.

The authors in [6] came to the same conclusion as in [12] when describing F_{es} at any given displacement point; only the former defined the gap distance between fingers in terms of the finger profiles, as seen in equation (2-9).

$$F_{es_Y}(Y_1) = \epsilon t \frac{V^2}{h(Y_1)} \quad (2-9)$$

2.4 Saw-Tooth Comb Drive

Jensen *et al.* [6] introduced numerical simulations for the sawtooth shaped unit comb drive. Although considered as simply a means to test their analytical model, the results from this simulation were used as the starting point in the development of the design presented in this report. Results from both the boundary element method and the original analytical model are shown in Figure 2.7.

This shape proved to be not-useful for resonant applications. However, the results shown by these authors were used as the first step in defining the shape introduced in the present research. Notice the arrows in Figure 2.7; the peaks occur when two outmost point-edges in both the movable and fixed sawtooth are exactly opposite to each other. If such one-dimensional points could be extended to two-dimensional areas, the force versus displacement response would show local maximum and minimum “plateaus”. Whenever these constant force values, i.e. plateaus, matched the restoring force of the micro-spring, the comb drive device would have *lock positions* before engaging further. This concept will be described in detail in the following chapters.

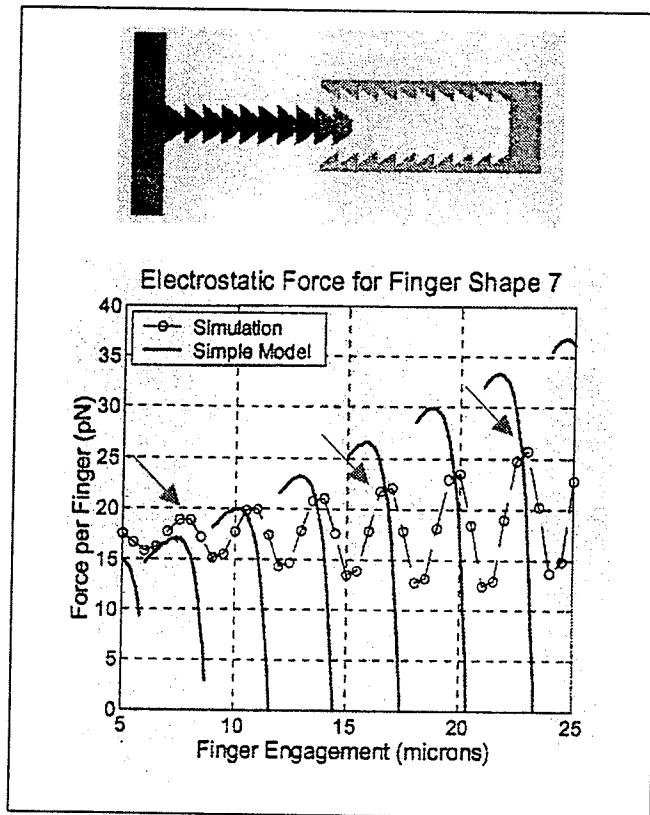


Figure 2.7. Sawtooth comb design and its characteristic force versus engagement plot from [6].

Part II – Microtweezers Actuation System

Mechanical microgrippers and microtweezers are useful in many current research areas. Such devices were developed as biological micromanipulators [14], [15], robotic grippers [16], [17] and general out-of-plane manipulators [18], [19]. Additionally, non-contact micromanipulation based on exposure to electric fields [20] and lasers [21], [22] have been developed as well.

This report focuses on describing an actuation device suitable for a microtweezers system. A successful microtweezers actuator must generate enough displacement to clasp the object of interest and keep a stable level of tension to hold on to the object. The sole open-close movement is not enough to guarantee the object will not slip from the gripping pads. Conversely, excessive closing force might damage the object of interest. Therefore, one might safely argue that the issue of controllability is imperative.

The following sections will briefly introduced some previously proposed actuation systems for use in microtweezers devices.

2.5 Thermal Actuation

The authors in [23] described microtweezers actuated by linear thermal expansion (Figure 2.8). This design takes advantage of thermal properties of single-crystal silicon, and thermal expansion is used for controlled mechanical work. Additionally, in order to

prevent normal displacement, the authors in [24] suggested the design should incorporate different-sized beams; these have an in-plane motion proportional to the amount of thermal energy applied to the device.

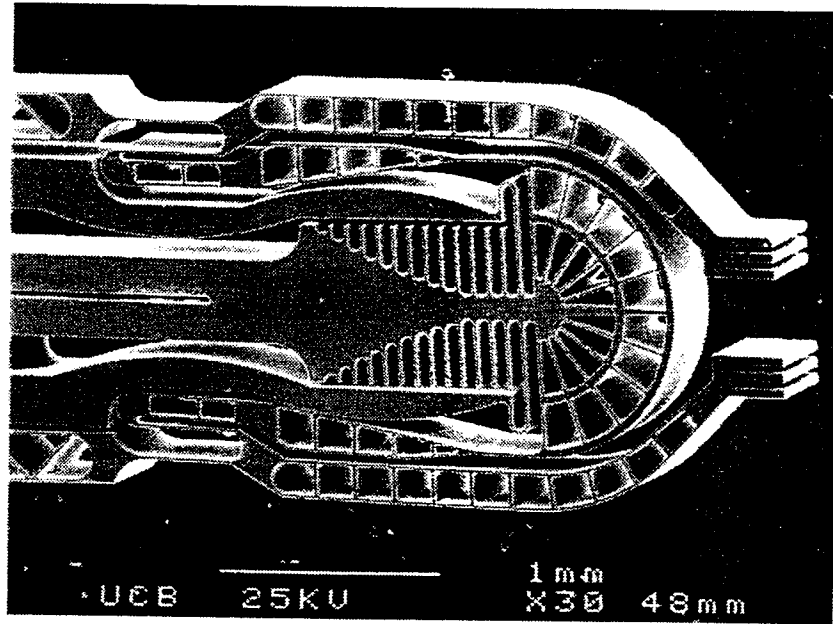


Figure 2.8. Thermally actuated microtweezers as described by Keller and Howe [23]. This picture has been downloaded from the author's website (www.memspi.com).

Thermal actuation is based on current flow and operational temperature is close to 200°C at 110mA [23]. Literature stresses the fact that special attention must be given to the design of thermal actuators in order to maximize the generated strain and the thermal isolation between the actuator and the gripping pads [5].

2.6 Electrostatic Actuation

The design presented by Kim *et al.* [14] makes use of flexible cantilever comb-drive arms with a bidirectional actuation. It must be noted that this adaptation of the original comb-drive design by [3] is prone to short circuit due to the differential displacement (Figure 2.9). Points *a* and *b* move in a semi-arc direction due to the cantilever bending moment. However, *b* covers a larger displacement distance and tends to snap shut against the fixed set of comb fingers. As a solution, the authors introduced an *over-range protector* kept at the same potential as the cantilever arm. The cantilever arm is kept at ground potential whereas the fixed set of fingers is at a given potential V .

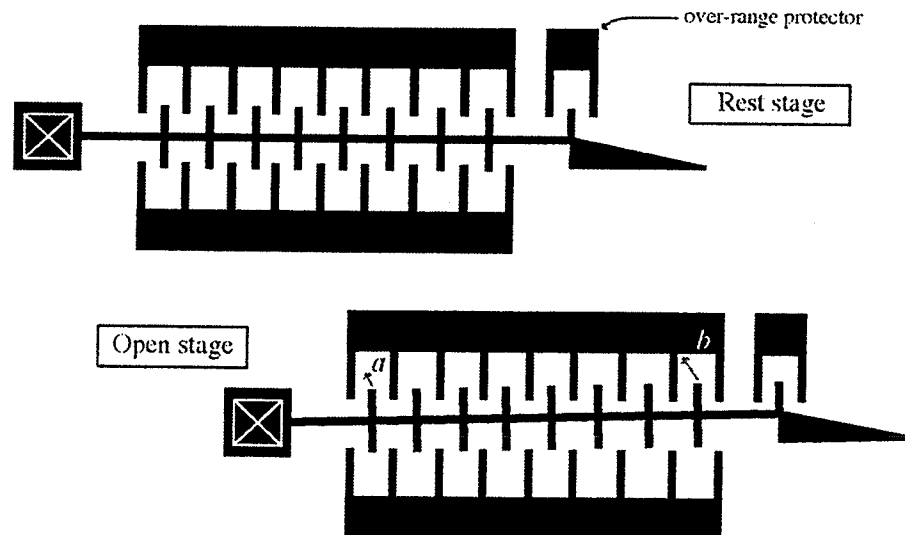


Figure 2.9. Drive mechanism for one of the two microtweezers arms for the device developed in [14]. Point *a* is closer to the cantilever pivot point and the total displacement at this point is less than that at *b*.

Chapter 2 Background on Comb Drives and Microtweezers

The authors reported smooth displacement of the gripper tip and low operational voltages (maximum 35V) for 40-finger comb drives. The relationship between applied voltage and movement of the gripper tip is quasi-linear from 0- to 7 μ m tip displacement. The remaining 3- μ m have a steep response to input voltage change. The controlling factor to prevent the cantilever arm from short-circuiting is the abovementioned over-range protector.

Chapter 3 Background on the Numerical Analysis of Comb Drives

This chapter will focus on introducing the background for the numerical analysis in the context of the comb drive simulation. The finite element method (FEM) was the method of choice for all the numerical simulations performed in this project. The information contained in this section supports the results described in the next chapter. The reader who is well versed in finite element analysis (FEA) in electrical and mechanical problems may choose to proceed to the next chapter. However, the reader who is unfamiliar with FEM is encouraged to read the concepts discussed in Appendix II.

3.1 General Description of the Problem

3.1.1 Electrostatic Analysis

The MEMS comb drive simulation is described as an *electrostatic problem*. Such a description is possible because electric charge can propagate through any dimension of the system under investigation in a time scale much shorter than the times of interest. The previous statement implies that the system response time is much slower than the time constants of the material. The Maxwell's equations relevant to the present simulations are simplified according to equations (3-1a-d).

Chapter 3 Background on the Numerical Analysis of Comb Drives

$$\left\{ \begin{array}{ll} \nabla \times \mathbf{E} = -\frac{\partial}{\partial t} \mu_0 \mathbf{H} \approx 0 & (a) \\ \nabla \times \mathbf{H} = \frac{\partial}{\partial t} \epsilon_0 \mathbf{E} + \mathbf{J} \approx 0 & (b) \\ \nabla \cdot \epsilon_0 \mathbf{E} = \rho_v & (c) \\ \nabla \cdot \mu_0 \mathbf{H} = 0 & (d) \end{array} \right. \quad (3-1)$$

The electrostatic problem discussed in this chapter can be physically described starting from Gauss' law:

$$\nabla \cdot \mathbf{D} = \nabla \cdot \epsilon \mathbf{E} = \rho_v \quad (3-2)$$

where,

$$\mathbf{E} = -\nabla V \quad (3-3)$$

It is assumed that the dielectric constant ϵ is continuous throughout the region surrounding the comb drive where the scalar potential field V is defined. Thus, the dielectric medium is homogeneous and the following substitution applies:

$$\nabla \cdot (-\epsilon \nabla V) = \rho_v \Rightarrow \nabla^2 V = -\frac{\rho_v}{\epsilon} \quad (3-4)$$

It follows that, since the comb drive is a capacitive device with air as the dielectric material, the region where the problem is defined is charge free ($\rho_v=0$). The electrostatic problem is then described by the Laplace equation (in rectangular coordinates):

$$\nabla^2 V = \frac{\partial^2 V}{\partial X^2} + \frac{\partial^2 V}{\partial Y^2} + \frac{\partial^2 V}{\partial Z^2} = 0 \quad (3-5)$$

Chapter 3 Background on the Numerical Analysis of Comb Drives

The goal of this chapter is to present and discuss the methods which will ultimately solve the Laplace equation. The objective is to find the potential distribution which satisfy equation (3-5) for a given electrode geometry at a predefined actuation potential V_0 . The potential distribution in the dielectric region is not known *a priori*. Since there is no current flow inside the comb drive device itself, the surface of the device is assumed equipotential.

Basic FEM theory states that a function can be approximated by a discrete model if and only if this function is continuous in the domain of interest [26]. Given that potential energy is a continuous quantity in the domain of interest, the fundamental requirement of the finite element method is met. The voltage-dependant continuous potential distribution can be approximated by a discrete model composed of a set of piecewise continuous functions defined over a finite number of subdomains. The discretization process approximates the partial differential equation (PDE) problem (Laplace equation) with a finite number of unknown parameters. This numerical solution will serve as input data into analytical equations, which will in turn produce results for *forces* and *displacements* in the system. The solution of the electrostatic problem serves as the *load force* to the mechanical problem. Both solutions combined give the desired comb drive characterization.

3.1.2 Mechanical Analysis

The mechanical analysis in this research aims at describing the double-folded cantilever beam spring deflection problem. As previously stated, the comb drive device is composed of two sets of capacitive fingers (movable and fixed) and the movable set is attached to a shuttle. This is the link between the electrostatic force-generating device and the two double-folded cantilever beam springs. Hence, the comb displacement is a combination of electrostatic pulling force, as seen in equation (2-4), and the mechanical spring restoring force (F_{mech}).

$$F_{mech} = k\Delta Y \quad (3-6)$$

Incidentally, equation (3-6) is defined for an incremental displacement in the Y-direction. In this section the second part of the comb drive problem, the spring restoring force, is described.

The following definitions apply to the cantilever springs: (a) the material used in the fabrication (polysilicon) is assumed homogeneous and isotropic; (b) the thickness dimension is small compared to the length; and (c) the stress in the normal Z-direction is ideally zero. It is nevertheless worth noting that in the actual environment the silicon substrate below the device causes a levitation phenomena that contributes to a finite Z-component of stress. In any case, levitation analysis is beyond the scope of this report and it is further described elsewhere [9]. The stresses and loads are defined in the X-Y plane and any other parallel plane has the same stress distribution. Thus, the springs fall

into the characteristic *plane stress* problem definition [25]. The variables of interest are the global spring displacements (u, v) in the X- and Y- directions. Normal stresses per unit element are:

$$\left\{ \begin{array}{l} \sigma_{XX} = \frac{F_X}{Area_{XX}} \quad (a) \\ \sigma_{YY} = \frac{F_Y}{Area_{YY}} \quad (b) \\ \sigma_{XY} = \frac{\mathbf{F}}{Area_{XY}} \quad (c) \end{array} \right. \quad (3-7)$$

where (a) and (b) stand for stresses in the X- and Y-directions, respectively. Equation (3-7c) states the shear stress given an applied total force with both X- and Y-components. The deformation per unit length in the X- and Y-directions are defined by the normal strains ϵ_{XX} and ϵ_{YY} respectively (3-8a-b). The shear strain per unit element of the spring material is shown in (3-8c).

$$\left\{ \begin{array}{l} \epsilon_{XX} = \frac{\partial u}{\partial X} \quad (a) \\ \epsilon_{YY} = \frac{\partial v}{\partial Y} \quad (b) \\ \epsilon_{XY} = \frac{\partial u}{\partial Y} + \frac{\partial v}{\partial X} \quad (c) \end{array} \right. \quad (3-8)$$

Finally, the stress-strain relations are defined from the constitutive relation of Hooke's Law, where E is the Young's modulus and ν is Poisson's ratio:

$$\begin{cases} \sigma_{xx} = \frac{E}{1-\nu^2}(\epsilon_{xx} + \nu\epsilon_{yy}) & (a) \\ \sigma_{yy} = \frac{E}{1-\nu^2}(\epsilon_{yy} + \nu\epsilon_{xx}) & (b) \\ \sigma_{xy} = G\epsilon_{xy} = \frac{E}{2(1+\nu)}\epsilon_{xy} & (c) \end{cases} \quad (3-9)$$

and G is shear modulus defined as:

$$G = \frac{E}{2(1+\nu)} \quad (3-10)$$

For a given beam with length ℓ , the boundary conditions for each beam are clamped-clamped, as seen in Figure 3.1. Equations (3-11a-b) are the mathematical description for both boundaries. Detailed formulation for a beam spring can be found elsewhere [27].

$$\begin{cases} Y(0) = 0 & Y(\ell) = 0 & \text{no deflection} & (a) \\ \frac{dY(0)}{dX} = 0 & \frac{dY(\ell)}{dX} = 0 & \text{no slope} & (b) \end{cases} \quad (3-11)$$

The solution for the spring problem is derived from Navier's equations for the X- and Y- components (3-12), where the vector \mathbf{K} represents the force applied to the shuttle, which in turn is connected to the springs and therefore acts as the load in this system. The stress tensor is represented by $\boldsymbol{\sigma}$, whereas $\mathbf{u} = (u, v)$ is the displacement vector. In the electrostatic case, the first term of the LHS equals to zero.

$$\rho \frac{d^2 \mathbf{u}}{dt^2} - \nabla \cdot \boldsymbol{\sigma} = \mathbf{K} \quad (3-12)$$

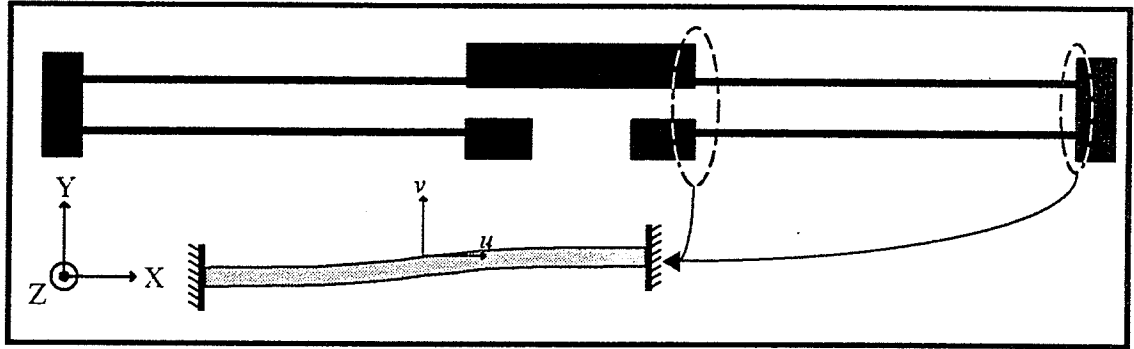


Figure 3.1. Schematic description of the spring beam boundary conditions.

3.2 The Arbitrary Lagrangian-Eulerian Formulation

3.2.1 Introduction

Comb drives are by definition transducers, which transform electrostatic energy into mechanical displacement. It implies that, in order to properly simulate the device, two domains must be coupled: the electrostatic domain and the mechanical domain. This is therefore characterized as a multiphysics problem. Simulation of such a problem through FEM is not trivial and difficulties arise in developing a mesh capable of approximating large deformations. Additionally, a dynamic parametric simulation generates increasingly deformed meshes, which in turn become unstable and solutions do not converge. The *Arbitrary Lagrangian-Eulerian* (ALE) technique is an advanced method of solving *moving boundaries* and *non-linear* problems in FEA [33], [34], [35]. The ALE method was chosen as a means to avoid such lack of convergence.

This technique makes use of the two FEM descriptions of motion: the *Lagrangian element* and the *Eulerian element*. Initial discussions on ALE were introduced by Hirt *et al.* [36]. Further developments were presented in [37], [38]. Basic ALE formulations are available from different sources [33], [39], [40], which can be used as an initial template and adapted to each specific problem. So far, ALE has not been widely used in the field of MEMS simulation; in fact, upon extensive research, only one paper was found which clearly applied ALE for solving a multi-domain MEMS problem [41].

Chapter 3 Background on the Numerical Analysis of Comb Drives

The ALE analysis technique uses an FE mesh that is neither attached to the material nor fixed in space. An arbitrary motion independent of the material deformation is assigned to each degree of freedom of the system. Special cases in the ALE numerical procedure may represent an Eulerian- or Lagrangian-only formulation. The main advantage of this technique lays in the fact that at any point of the analysis a solution may be computed, both in cases where large and highly localized deformation of the structure occur, and where unconstrained flow of material on free boundaries happens. When free boundaries exist, the ALE may be reduced to a Lagrangian form; if large deformations occur at any point of the analysed geometry, than the solution algorithm takes the Eulerian form.

One characteristic of the ALE formulation is that the solution variables representing structural deformation are only determined at elements within the structure boundaries. The coupling with other simulation variables happens through the mesh displacement characteristics. Thus the structure deformation properties must be transferred to mesh points through an updating algorithm. Additionally, prescribed mesh displacements must be assigned for all degrees of freedom of the mesh, at each iteration of the numerical solution [30].

For the purpose of this report, the reader should familiarize himself with the following concepts:

- The ALE method is applied to the electrostatic problem as a way to deal

with the constant rearrangement of field lines as a function of comb movement.

- Recall that the electrostatic problem is defined in the dielectric surrounding the comb drive. The ALE discussions refer to the dielectric domain as the *dielectric material structure*, or simply *dielectric material*. This corresponds to the entire area surrounding the comb drive minus the comb drive itself.
- The solutions of the ALE simulation are used as loads in the plane stress simulation mode.

In what follows a description of ALE in the context of the comb drive simulation will be introduced. The algorithm is discussed with the aim of demonstrating the robustness for solving large deformation problems without losing convergence.

3.2.2 The ALE and the Comb Drive Simulation

The ALE formulations are based on two sets of coordinate systems [42]. The first coordinate system is attached to the dielectric material and it trails the deformation of the field lines defined in the material. This system is identified by the variables X, Y, Z . A second coordinate system defines a computational mesh, which moves according to pre-defined mesh displacements. The computational mesh is identified by x, y, z in rectangular coordinates. The reader should be careful not to confuse the FE mesh and the ALE computational mesh. For the sake of clarity, the ALE computational mesh will henceforth be referred to as *computational grid* or simply *the grid*.

A one-to-one mapping between the dielectric material displacements and the grid movement must exist. That requires that both domains coincide and all displacements happen inside the domain borders, which implies in the identity shown in (3-21);

$$(\bar{\delta} - \delta) \cdot \mathbf{n} = 0 \quad (3-13)$$

where $\bar{\delta}$ and δ corresponds to the grid displacement and the dielectric material displacement, respectively. Figure 3.2 offers a graphical interpretation of the previous statement.

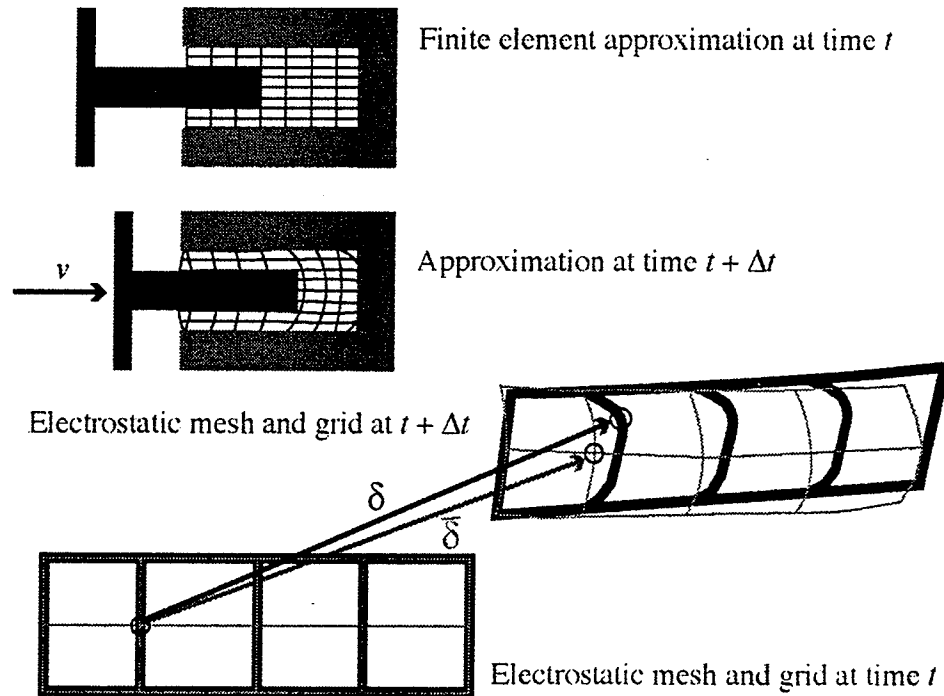


Figure 3.2. This is an illustrative demonstration of the interaction between the electrostatic problem and the ALE grid displacement.

The logical outcome of the implementation of (3-21) is as follows: the algorithm performs an automatic grid re-design procedure, which maps the original domain into the deformed domain at each displacement instance. Hence the ALE formulation specifies

which boundaries will move during the simulation and how they should move. Previous sections described the characteristics of independent electrostatic and plane stress simulation. With ALE, both simulations are performed together and the solution of one part serves as a boundary condition to the second part. Thus, the ALE formulations can be described as an algorithm that performs automatic reasoning [43], according to the following steps:

1. When the grid is distorted enough and convergence is no longer possible, calculations are stopped.
2. Grid is smoothed.
3. Last solution achieved from the distorted grid is remapped into the new, smooth grid.
4. Calculations are resumed.

Step 1 is related to the issue of *element quality* described in section **Error! Reference source not found.** The software package automatically defines a threshold where a significant number of low quality elements prevent the successful determination of a solution. The four steps described above suggest an implicit incremental approach [39]. In the case of this thesis, all solutions are derived from a parametric analysis, where the parameter is the input actuation potential V_0 , as described in detail in Chapter 5. At all iterations, it is assumed that the governing equations of the problem under scrutiny are in equilibrium. Hence the solution for the equilibrium equations in the ALE formulation are already known for all parameter steps from $V_0 = 0$ until $V_0 = V$. Each subsequent

iteration i solves for the next parameter step $V_0 + \Delta V$. The vector equation (3-22) represents the previous statement, where δ is any arbitrary 2D field line displacement.

$$V_0 + \Delta V \delta_{(i)} = V_0 \delta_{(i-1)} + \Delta V \delta_{(i)} \quad (3-14)$$

3.2.3 Problem Definition

The device analysed in this research is qualified by its strong monotonicity property, dielectric material linearity and geometrically nonlinear behaviour. The nonlinearity stems from the large deformation that the field lines undergo whilst the device engages. This consequently produces a problem with moving boundaries. The ALE algorithm is carried out as a means to manage the continuous changes in the field lines without losing convergence. The successful solution of each ALE iteration serves as input load to the coupled mechanical displacement problem.

Proper implementation of the ALE algorithm depends on two conditions: (a) the topology of the geometry must be the same throughout the simulation, and (b) there exists an appropriate PDE which characterizes the computational grid prescribed displacement [39]. The implementation of ALE starts from characterizing a mapping function from the original domain Ω into a deformed domain $\bar{\Omega}$:

$$f : \Omega \mapsto \bar{\Omega} \quad (3-15)$$

where (x,y) represents the deformed coordinates defined in terms of the fixed X- and Y-

axes and in time t , as per the definitions in (3-24).

$$\begin{cases} x = f(X, Y, t) & (a) \\ y = f(X, Y, t) & (b) \\ (X, Y) \in \Omega & (c) \\ (x, y) \in \bar{\Omega} & (d) \\ t \in \text{Re}^+ & (e) \end{cases} \quad (3-16)$$

Since the comb drive problem requires information on grid *displacements*, rather than solely grid coordinates, the deformed domain variables are redefined according to (3-25). Figure 3.3 offers a general understanding of the intended steps in the ALE implementation.

$$\begin{cases} x = X + \delta x \\ y = Y + \delta y \end{cases} \quad (3-17)$$

The ALE formulation guarantees the independency of the computational grid movement from the electrostatic field movement and it still recovers a homogeneous mesh at each iteration. The development of local stiffness matrices requires a transformation matrix \mathbf{T} that relate the displacements δ in the deformed coordinate system to the fixed coordinate system as described below:

$$\begin{cases} [\delta(x, y)]\mathbf{T} = [\delta(X, Y)] \\ [\delta(x, y)] = [\delta(X, Y)]\mathbf{T}^{-1} \end{cases} \quad (3-18)$$

The derivatives of the electric field nodes coordinates are computed in the

Chapter 3 Background on the Numerical Analysis of Comb Drives

$(X,Y) \in \Omega$ domain, but the element displacements, or distorted grid, have been previously defined in the $(x,y) \in \bar{\Omega}$ domain. Thus, in order to recover the shape functions in the undeformed domain, the *chain rule of derivatives* must be used, which relates the (x,y) coordinates back to the (X,Y) and the appropriate incremental displacement can be calculated. It turns out that the transformation matrix \mathbf{T} at each node with respect to the fixed coordinate system is the *Jacobian* matrix \mathbf{J} , and the inverse Jacobian \mathbf{J}^{-1} must be computed, according to the identity (3-27).

$$\mathbf{J} = \begin{bmatrix} \frac{\partial x}{\partial X} & \frac{\partial x}{\partial Y} \\ \frac{\partial y}{\partial X} & \frac{\partial y}{\partial Y} \end{bmatrix} = \begin{bmatrix} \frac{\partial}{\partial X}(X + \delta x) & \frac{\partial}{\partial Y}(X + \delta x) \\ \frac{\partial}{\partial X}(Y + \delta y) & \frac{\partial}{\partial Y}(Y + \delta y) \end{bmatrix} = \begin{bmatrix} 1 + \frac{\partial}{\partial X}\delta x & \frac{\partial}{\partial Y}\delta x \\ \frac{\partial}{\partial X}\delta y & 1 + \frac{\partial}{\partial Y}\delta y \end{bmatrix} \quad (3-19)$$

$$\mathbf{J}^{-1} = \frac{1}{\det \mathbf{J}} \begin{bmatrix} 1 + \frac{\partial}{\partial Y}\delta y & -\frac{\partial}{\partial Y}\delta x \\ -\frac{\partial}{\partial X}\delta y & 1 + \frac{\partial}{\partial X}\delta x \end{bmatrix} \quad (3-20)$$

As previously stated in section 3.2.2, the one-to-one mapping depends on a non-zero Jacobian [30] and the boundaries of the two domains (structural and mesh) must coincide. The detailed description of the ALE method implementation in the comb drive analysis can be found in Part II of Chapter 5.

3.3 Conclusion

Chapter 3 has described numerical principles used to simulate the comb drive problem. Two types of analysis were investigated; initially the comb drive simulation was presented as two independent problems, namely the electrostatic and the mechanical components. This analysis is described in three dimensions and its governing equations were introduced. The basis of the finite element method was established and discussed in the context of the comb drive simulation.

This initial discussion led to the presentation of the Arbitrary Lagrangian-Eulerian formulation as a practical numerical tool to integrate both electrostatic and mechanical problems. The ALE method was considered as an innovative way to deal with multiphysics analysis in MEMS simulation problems. This technique was discussed in a two-dimensional viewpoint.

Chapter 5 will present the application of the techniques discussed here. The reader will also find an examination of the results achieved with the abovementioned numerical methods.

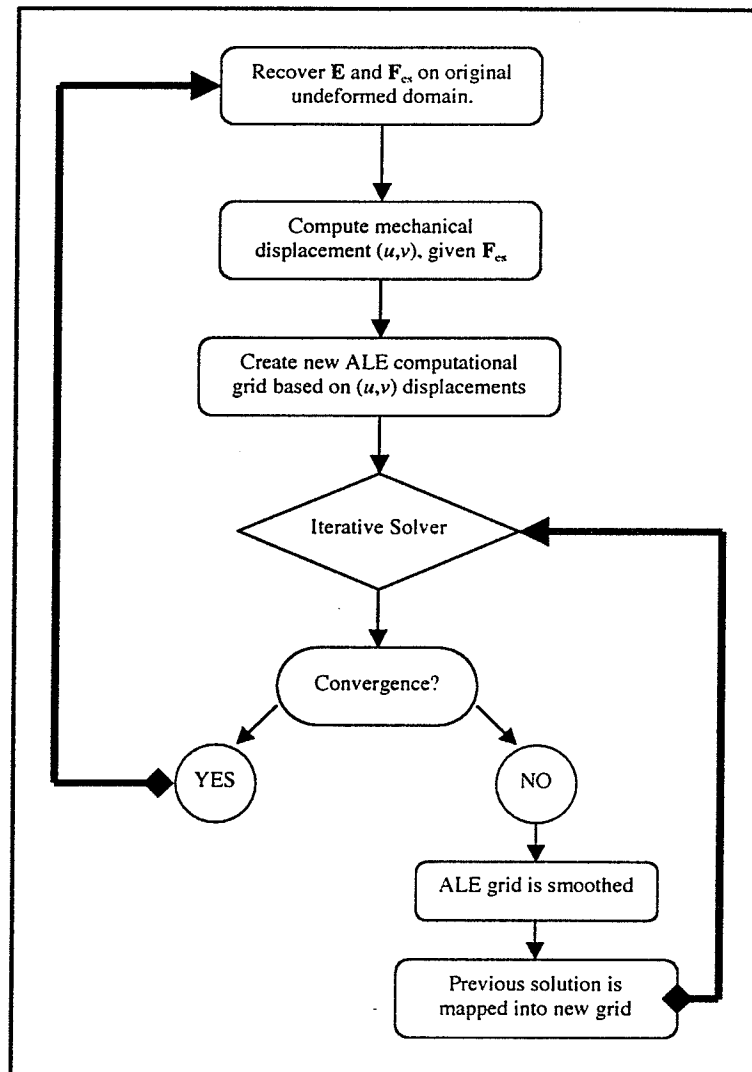


Figure 3.3. Flowchart describing the ALE procedure.

Chapter 4 Fabrication and Initial Testing

4.1 Preamble

The design of the comb drives was based on standard geometries available through the Multi-User MEMS Processes (MUMPs). The whole of the device was defined in one single polysilicon layer and the 2- μm structural thickness followed the fabrication design standard. This chapter will discuss steps in the fabrication process relevant to the target design. Additional detailed descriptions of design rules in MUMPs are available in [7].

The rectangular resonant comb-drive design (Figure 2.1) is available in the MUMPs library of masks. It was used as an initial template for the other two designs tested: jagged-edge and sawtooth shapes. The dimensions of each comb finger set are described in Figure 4.1. Due to issues related to chip real state availability, the fabricated springs followed the standard 140- μm -long MUMPs design (Figure 4.2).

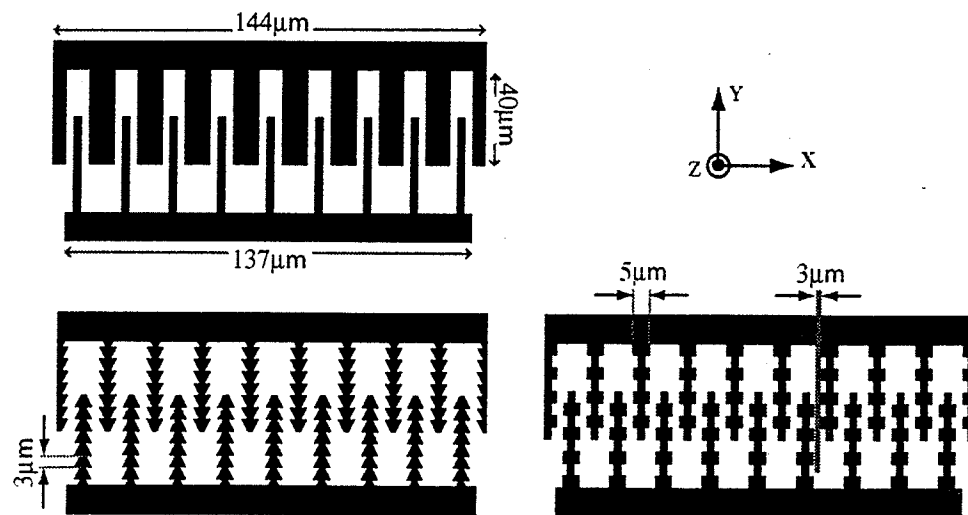


Figure 4.1. View of the X-Y plane of the three simulated comb shaped. From top to bottom: rectangular, sawtooth, and jagged-edge.

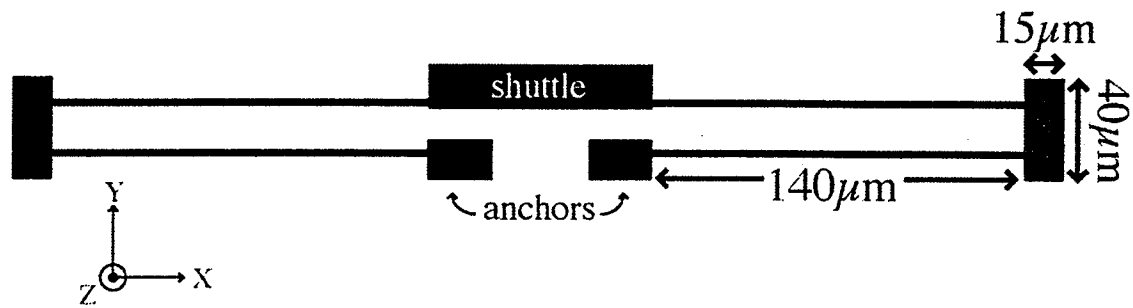


Figure 4.2. Schematic description of the fabricated spring. The shuttle is the mounting structure where the comb drive is attached.

4.2 Design Considerations

The design features were adapted to best suit the requirements of the MUMPs process. The minimum distance between features accepted by the MUMPs design rule check was $2\text{-}\mu\text{m}$. Nevertheless, due to the irregular nature of both the jagged-edge and the sawtooth designs, an extra $1\text{-}\mu\text{m}$ was introduced in the gap between fingers, for a final $3\text{-}\mu\text{m}$ gap. This was used as an artifice to prevent the risk of having fused features, mainly due to imprecision in the photoresist layer.

On the other hand, in order to guarantee the convex corners at each jagged or sawtooth notch, compensating extended features should have been added to each notch edge [44]. Such features should prevent loss of resolution in the lithography step, but the mask requirements are such that the introduction of compensating corners would not fit the MUMPs design flow. It was decided that compensating corners would not be added to the mask design. Hence, it was known in advance that the convex corners would be attenuated in the final device. This attenuation would eventually add to the gap distance between fingers.

4.3 Fabrication Procedures

The mechanical properties of the polysilicon layer used in the MUMPs run depend on the fabrication run and foundry specifications. For the purpose of this thesis, the values adopted for numerical simulations were according to [45] and are displayed below:



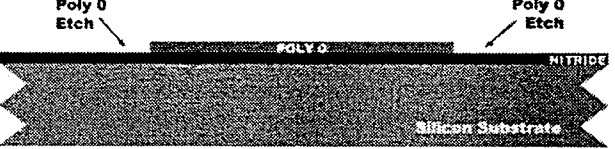
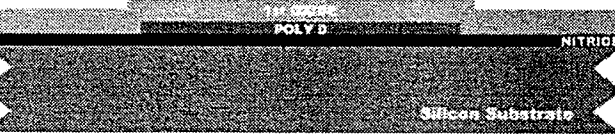
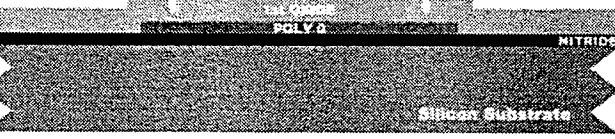
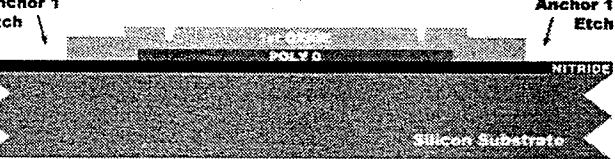
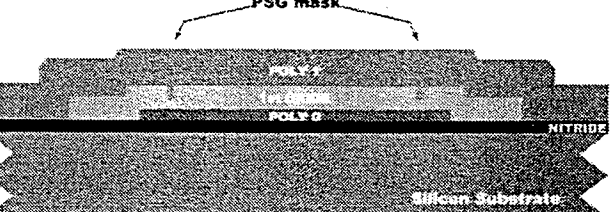
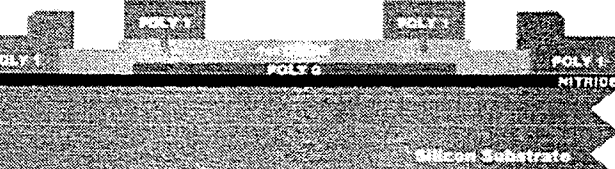
Young's Modulus [E] 158 ± 10 GPa

Poisson's Ration [ν] 0.22 ± 0.01

The MUMPs fabrication process has three layers of polysilicon, where the two top ones are used as structural layers. The comb drives are all designed in one single structural layer, POLY1. The fabrication method used for layer deposition is the *low pressure chemical deposition* (LPCVD) and etching is done through *reactive ion etching* (RIE). The sacrificial layer used is *phosphosilicate glass* (PSG), which is removed in the final step of the process, at which point the mechanical structures are released.

The first step, phosphorus doping, prevents charge feedthrough to the wafer substrate, whereas the nitride is deposited as an electrical isolation layer. Table 4-1 introduces the steps leading to the fabrication of the comb drives. The metal layer is second last step and final deposition layer. A 0.5- μm gold and adhesion layer is deposited via lift-off. This method does not require etching. The remaining steps in the design flow can be found in [7]. All masks were designed in Cadence 5.0 [46] and subjected to the MUMPs design rule check available in the software package library.

Table 4-1. MUMPs process flow. The steps described here are those relevant to the comb drive fabrication. All schematics are from [7].

PROCESS	DESCRIPTION	SCHEMATICS
1. Doping 2. LPCVD 3. LPCVD	POCl ₃ serves as a source for P; 600-nm Si ₃ N ₄ layer for electrical isolation. 500-nm polysilicon layer (POLY0)	
4. Lithography	Patterns the resist.	
5. RIE	Etches POLY0	
6. LPCVD	2-μm sacrificial layer of PSG	
7. Lithography 8. RIE	Resist is patterned. The pattern is transferred into PSG	
9. Lithography 10. RIE	Anchors for first structural layer are etched.	
11. LPCVD	2-μm layer of POLY1 (structural layer). Followed by 200-nm layer of PSG	
12. Lithography 13. RIE	The PSG layer is patterned with lithography and structural design is transferred to POLY1.	

4.4 Design Results

The final fabricated devices (Figure 4.3-5) proved extremely sensitive to the variations in geometry introduced to the design. The expected square notches at the jagged-edge comb drive were considerably smoothed down at the edges, giving it a final rounded shape. Similar results happened with the sawtooth comb drive, where the tip of each notch was also smoothed down. It was expected that such discrepancies from the original design would play a significant role in the final test results, departing the experimental results from the FEM numerical solutions.

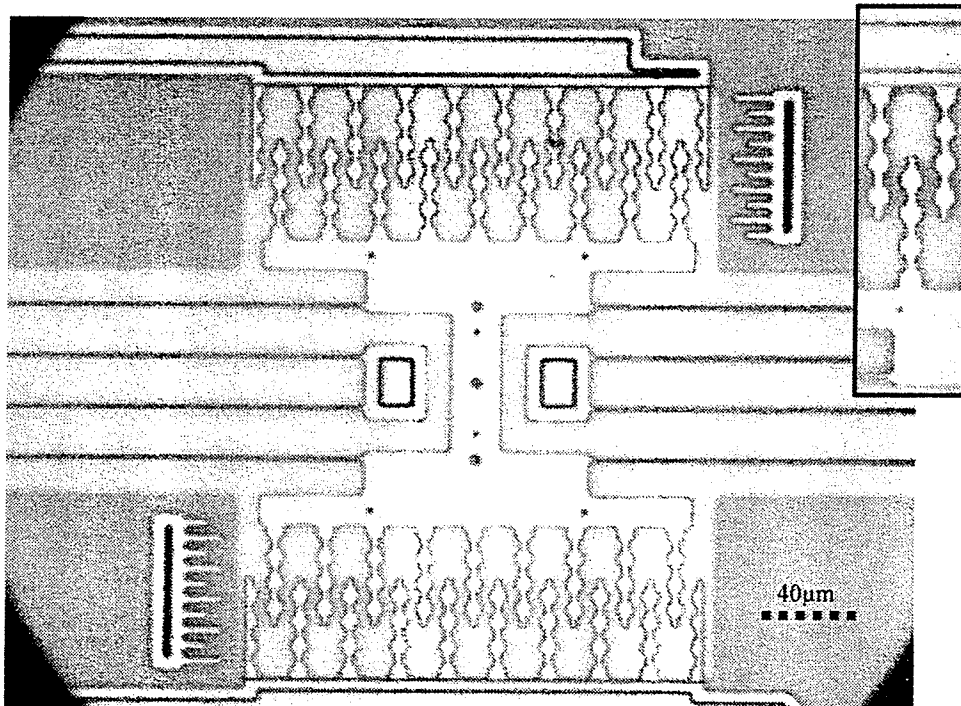


Figure 4.3. Jagged-edge shape comb drive viewed through a 50X enlargement objective. The detail shows the 100X enlargement of a unit comb finger.

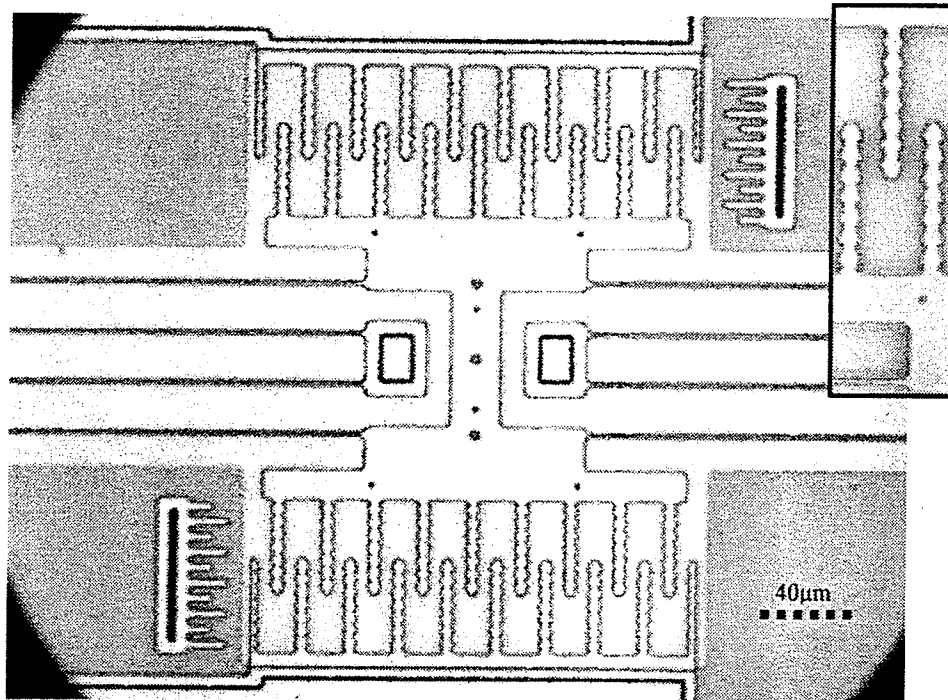


Figure 4.4. Sawtooth shape comb drive viewed through a 50X enlargement objective. The detail shows the 100X enlargement of a unit comb finger.

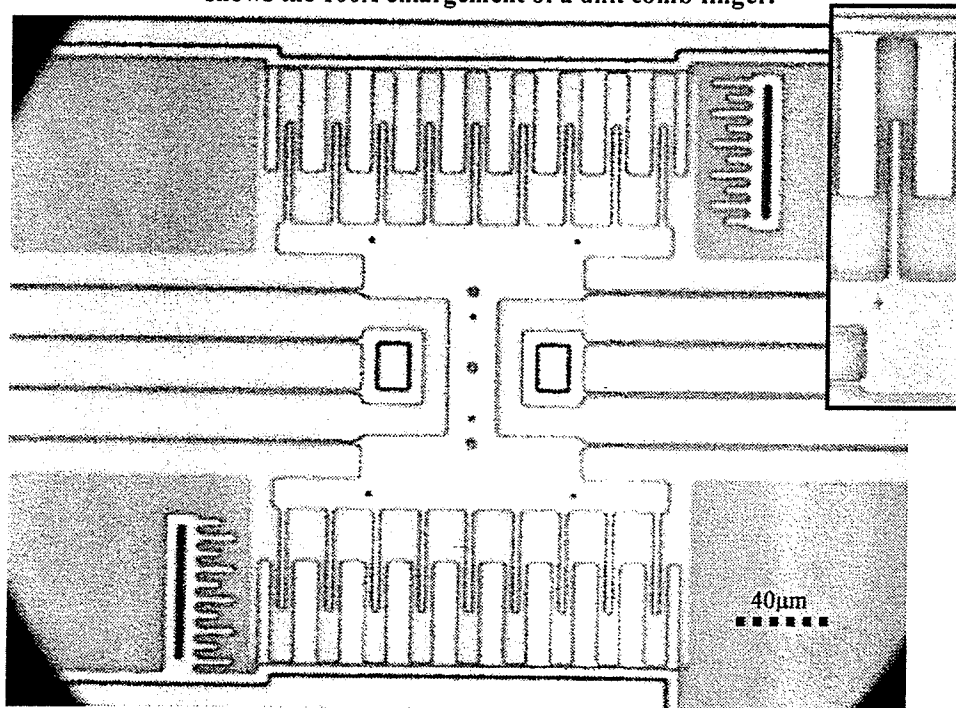


Figure 4.5. Rectangular shape comb drive viewed through a 50X enlargement objective. The detail shows the 100X enlargement of a unit comb finger.

4.5 Testing

Based on the theory discussed so far, it is known that the performance of the comb drive design is based mainly on the following factors: total number of capacitive fingers; sidewall dimensions in each finger, finger gap distance, spring dimensions and actuation voltage bias (please refer to Table 2-1 for more details). Additionally, in a testing environment, issues such as input signal noise, and ground plane interference do play a role.

The devices were tested with the use of manual, linear motion surface probes by Wentworth Laboratories. Three probes were used at each test run. They were connected to the metallized actuation pads of the comb drive under test. Two grounded probes were connected to the shuttle and one set of fixed-finger. The remaining set of fixed fingers was probed at a given potential V_0 . The actuation voltage was supplied by two Agilent E3647A voltage sources of 0- to 60V in series, according to the schematic in Figure 4.6.

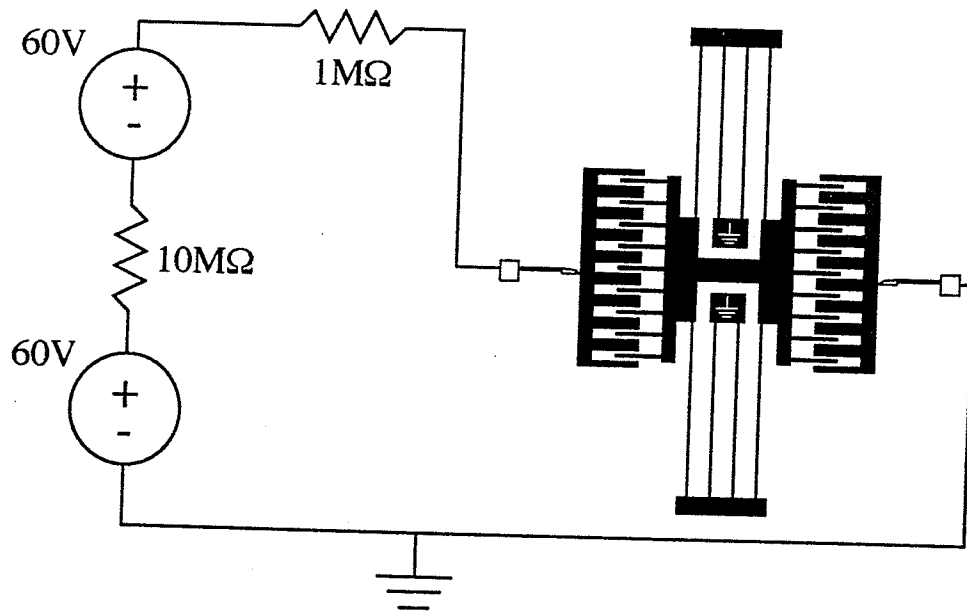


Figure 4.6. Schematic description of the testing environment. The shuttle shared the same ground as one of the fixed fingers.

The rectangular comb drive had total lateral displacement of $9\mu\text{m}$ in each direction. This constituted the best displacement results of all tested devices, since the sawtooth comb drive had only a $3\text{-}\mu\text{m}$ lateral displacement and the jagged-edge device engaged only one $5\text{-}\mu\text{m}$ notch. However, given the difficulties in implementing the design, this 1-notch engagement was enough to show the viability of the design.

An optical microscope Olympus BX51 with 50X and 100X objectives was used to follow the behaviour of the device during testing. It was noted that the entire device was not in complete focus at any one time. This led to the conclusion that, given the amount of adjustment necessary to refocus the object, the movable and fixed sets of fingers were out of plane. It is speculated that after the release step in the fabrication process, thin film stresses caused the device to be out of plane.

4.6 Conclusion

Improvements in the design are clearly necessary. Given the minimum dimensions required, the MUMPs fabrication was not very effective in achieving the proposed designs. However, a simple increase in spring length could improve significantly the comb drive response to the DC actuation voltages applied, as it will be discussed in section 5.5 of the following chapter. The fact that the comb fingers were out-of-plane was not expected and it did add an extra difficulty to the test procedures. A bias voltage could be introduced to the movable fingers and an optimum overlap could be achieved to overcome the out-of-plane issue. However, at this point it was clear the design would need improvements and thorough simulation was required.

The following chapter will discuss the mathematical simulation of the devices. That should render a more complete understanding on why the device with the present dimensions is not effective and how that can be improved.

Chapter 5 Design Simulations and Numerical Solutions

5.1 Preamble

All finite element simulations were performed in the FEMLAB 3.0a [47] software package. Both two- and three-dimensional problems were analyzed. The numerical analysis was divided into two parts. Part I describes two independent three-dimensional simulations performed for the electrostatic comb fingers and the mechanical spring problems. The numerical solutions obtained through FEM simulations were input into analytical models and a final solution was generated. This combined method reconstituted the comb drive problem, but the independent characterization of each part did not return a complete description of the device.

Part II was based on a thorough numerical solution of the comb drive as a whole: comb fingers and springs together. In this case, symmetry was used to retrieve solutions from two kinds of two-dimensional problems: the rectangular and jagged-edge comb drives. The standard numerical tools available in FEMLAB 3.0a were not sufficient to analyse the combined problem, thus the Arbitrary Lagrangian Eulerian technique was applied. A detailed description of the procedures of each simulation is described in this chapter.

5.2 Mesh Generation

The nature of this work is comparative in the sense that each simulation run must be analysed with respect to each other. Thus, the objective of the meshing stage is to achieve a mesh which can be reasonably matched among all simulations.

The automatic mesh generator in FEMLAB 3.0a was used to create optimized meshes. However, in order to evaluate the quality of results achieved, an initial *mesh quality analysis* was performed for a 2D rectangular comb drive. Electrostatic simulations were performed for several different mesh densities for linear and quadratic elements. The densities chosen followed the standard values available in FEMLAB 3.0a varying from *extremely coarse* to *extremely fine* densities. The goal of this analysis was to calculate the total capacitance under the same conditions, using different mesh densities. Figure 5.1 shows that quadratic elements returned similar results irrespective of mesh density. As for the linear elements, results varied close to 14% when compared to quadratic elements. Additionally the correlation between mesh density and solution accuracy did not prove to be conclusive in the case of linear elements. Based on these results, all simulations presented in this chapter were derived from FEMLAB's automatically generated "coarser" mesh using quadratic elements.

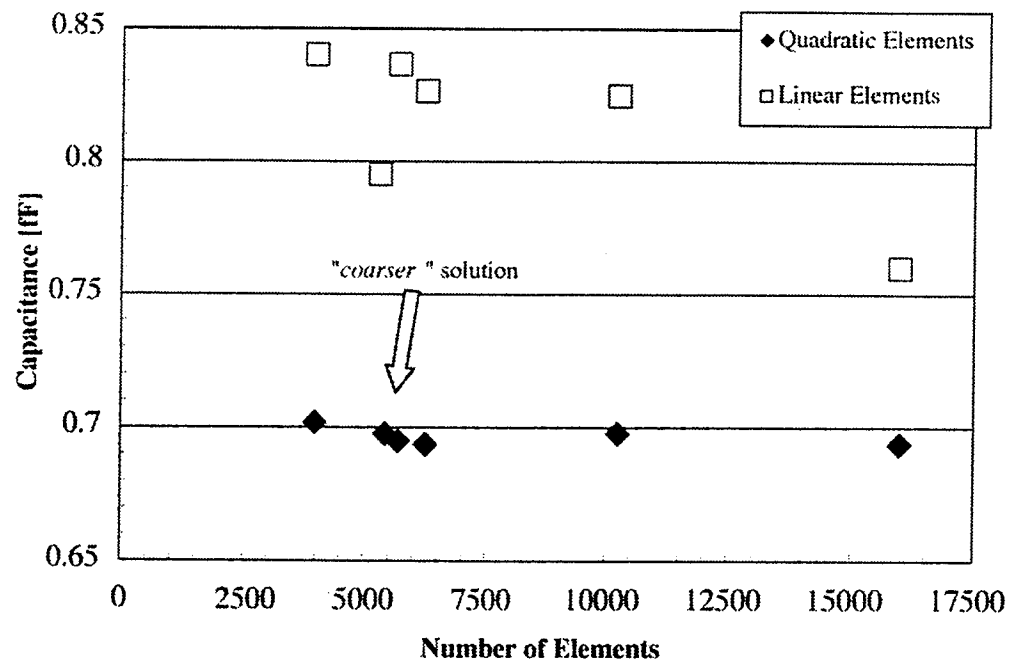


Figure 5.1. Mesh density analysis. The arrow points to the “coarser” mesh solution.

Detailed and systematic *error analysis* in FEM was considered beyond the scope of this text. The reader is suggested to pursue further readings on the subject [48] [49], particularly related to electrostatic FEA [50] [51]. Nevertheless, all simulation runs were preceded by an element *quality analysis* (details on quality analysis can be found in Appendix II). Figure 5.2 shows a quality histogram for one case study of mesh element quality. In the case of 3D analysis, the tetrahedral element is considered reliable for all those elements with quality above 0.3. As for the 2D models, the triangular element should have quality above 0.6 [52].

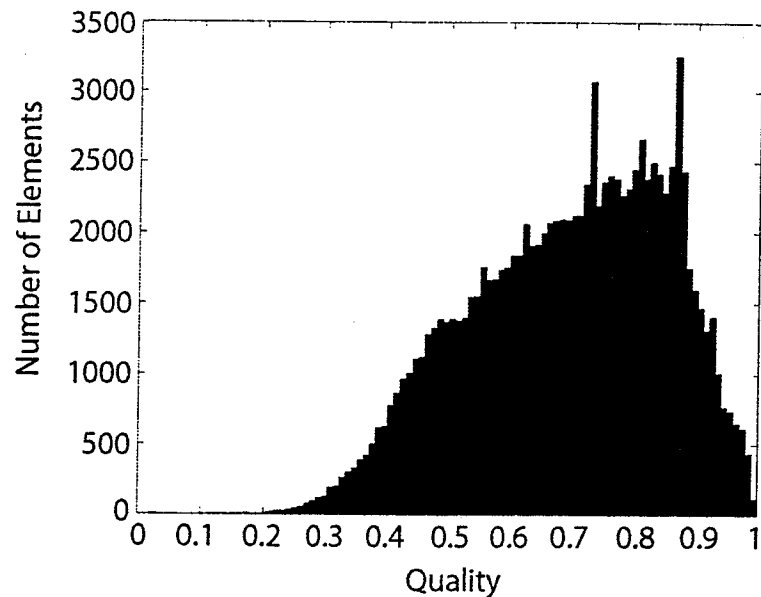


Figure 5.2. Example of a quality histogram for the FEMLAB automatic *coarser* mesh analysis with quadratic element. This case study is based on a 2D rectangular comb drive.

The solver algorithm used in the mesh quality analysis was the default *Direct Linear*, which is the standard solver in the FEMLAB electrostatic application mode. For the purpose of this report, independent benchmark tests performed elsewhere [53] were considered as enough proof of reliability in FEMLAB results. Hence, all solver algorithms used were based on the default options in the package for each multiphysics application mode.

Part I – Independent 3D Simulation

Figure 5.3 defines the procedure followed in each independent simulation as well as it explains the connections between the electrostatic input variable, the electrostatic solution variable and its link with the mechanical analysis. The FEM solution from the electrostatic problem was used to calculate the total capacitance created by the comb fingers in parallel. The capacitance value served as input for the electrostatic force analytical model. The result was used as the *load* force to which the springs were submitted in the FEM analysis. Next, the maximum displacement of the springs due to the given load was computed and used to determine the linearity of the spring, combining equations (2-4) and (3-6). With these results, the mechanical force necessary for a given extension of the springs was calculated.

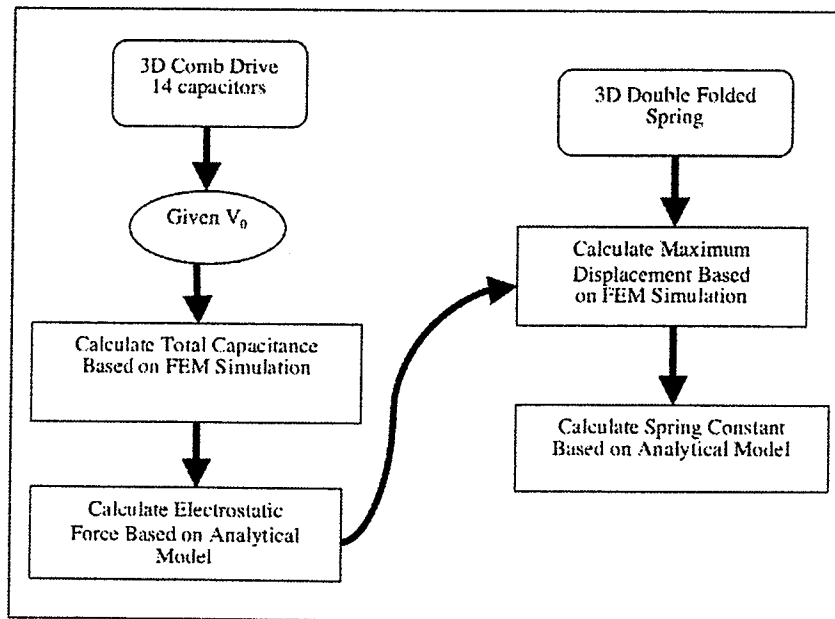


Figure 5.3. Independent electrostatic (left column) and mechanical analysis (right column).

Sections 5.3 - 5.5 will discuss electrostatic and mechanical analysis separately and the results of simulations will be combined. A preliminary characterization of the comb drive device is discussed.

5.3 Electrostatic Simulation

The set of 10-fixed and 9-movable fingers form a group of 18 capacitors in parallel. The design was imported into FEMLAB as a standard *dx*f file and extruded to 2- μ m thickness (refer to previous Figure 4.1). The surrounding dielectric subdomain was simulated by an “air-filled” solid with 27- μ m in thickness, 135- μ m in width and 235- μ m in length. These dimensions were chosen such that the distance between the surrounding dielectric boundaries and the device boundaries would remain at a constant 25- μ m length.

Since geometry cannot be treated as a variable parameter, individual runs were made for each comb engagement, that is, the movable set of fingers was displaced from the initial rest position¹ at 20- μ m to the final 39.5- μ m displacement. Each run represented an increment in 2- μ m in the Y-direction. Additional runs were performed for the *negative engagement* case, when fingers were retracted to a position preceding the rest position. For computational simplicity the short-circuit situation, where the movable fingers touch the fixed fingers, was avoided. An intentional 0.5- μ m gap was left in the

¹ The reader should note that, henceforth, for the purpose of plots describing finger displacement, the initial rest position is always at 20- μ m engagement. Displacement values below 20- μ m correspond to *negative engagement* or simply retraction of the springs.

maximum engagement situation; therefore, new boundary conditions were not needed. Three-dimensional simulations were performed in three independent sets of comb finger, henceforth referred to as *jagged-edge* shape, *rectangular* shape and *sawtooth* shape. Figure 5.4 represents three examples, all at 26- μm engagement for each of the tested shapes.

At this point, the main goal was to understand the differential capacitance with respect to engagement. As previously shown in equation (2-1), capacitance is independent from actuation voltage, hence an initial input test voltage $V_0=1\text{V}$ was used. Upon achieving a solution for all displacements, total capacitance was computed via *subdomain integration* according to equation (2-2).

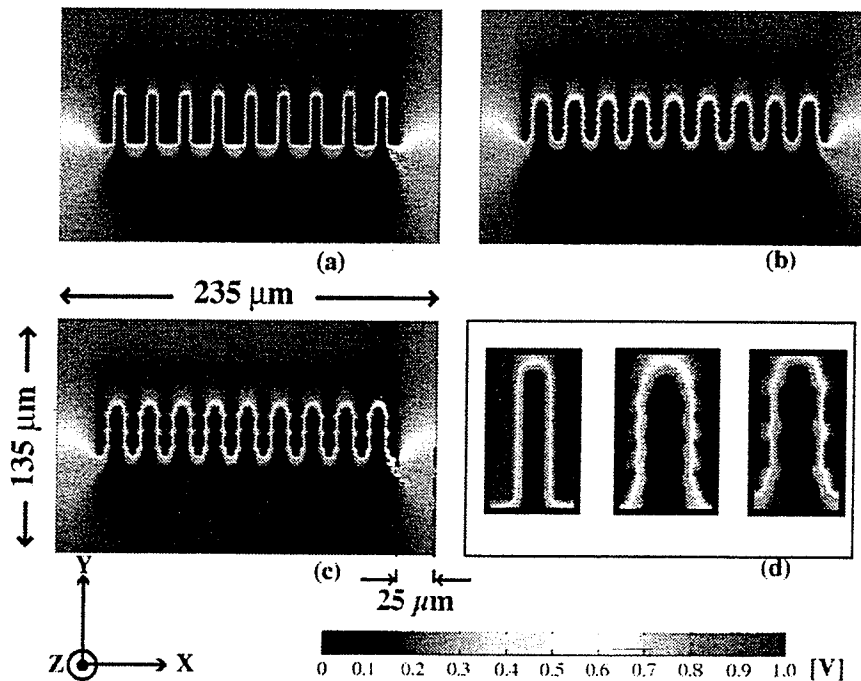


Figure 5.4. Potential field distribution results for a 26- μm engagement of three different comb finger shapes. The dimensions of the total integration area are shown in (c). Excerpts (d) depict the details of field distribution around each finger.

Chapter 5 Design Simulations and Numerical Solutions

The numerical solution for differential capacitance was computed following equation (5-1), where C_{TOT} is the total capacitance at each engagement increment n . This works as the *Principle of Virtual Work* (PVW), extensively reported in literature. A concise description of PVW can be found in Appendix I.

$$\begin{cases} \left[\frac{\partial C_n}{\partial Y} \right]_{((n-1) \times 1)} = \left[C_{TOT_n} - C_{TOT_{(n-1)}} \right]_{((n-1) \times 1)} & (a) \\ \left[\frac{\partial C_n}{\partial Y} \right] = \left[\frac{\partial C_n}{2 \times 10^{-6}} \right] & (b) \end{cases} \quad (5-1)$$

We can see that this capacitance equation increases linearly with finger displacement (Figure 5.5). The total capacitance of the rectangular shape comb was, in average, 28% higher than that computed from the sawtooth shape and 13% higher than the jagged-edge shape. As expected, the capacitance recovered from the 3D models were higher than those computed from the 2D model due to fringing. Figure 5.6 confirms the suggestion that fringing fields are indeed prevailing in this design, most likely because the distance between the capacitor plates is $1\mu\text{m}$ larger than the thickness of the structure. The streamlines were randomly displaced through the comb drive device in order to emphasize the fringing fields at both lateral edges. That invalidates the theoretical assumption of parallel plates capacitors, where fringing fields can be neglected in the calculation of total fields.

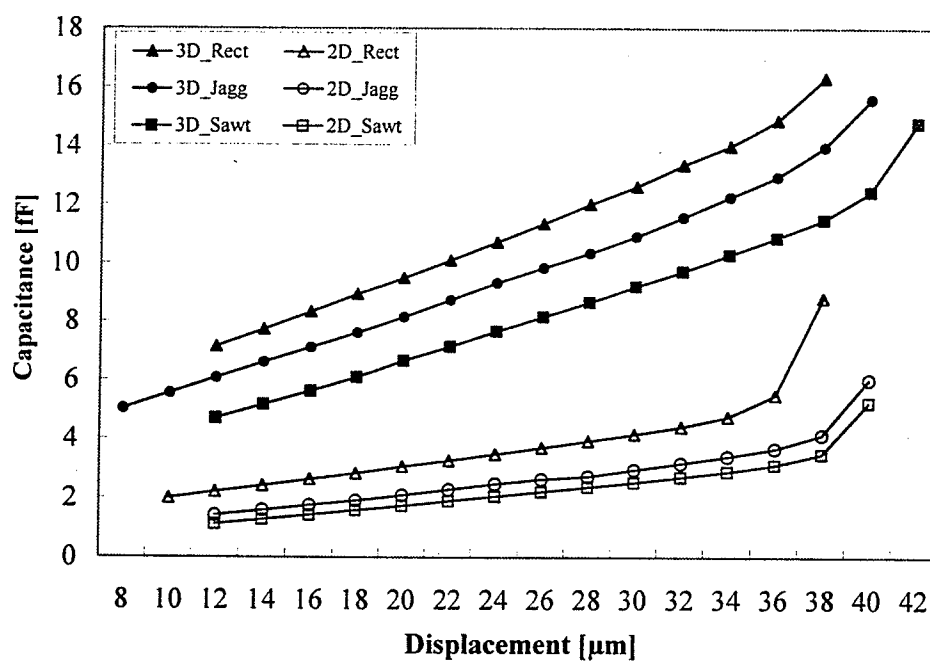


Figure 5.5. The bold shapes represent total capacitance values recovered from the 3D simulations. The hollow shapes represent total capacitance values from the 2D simulations.

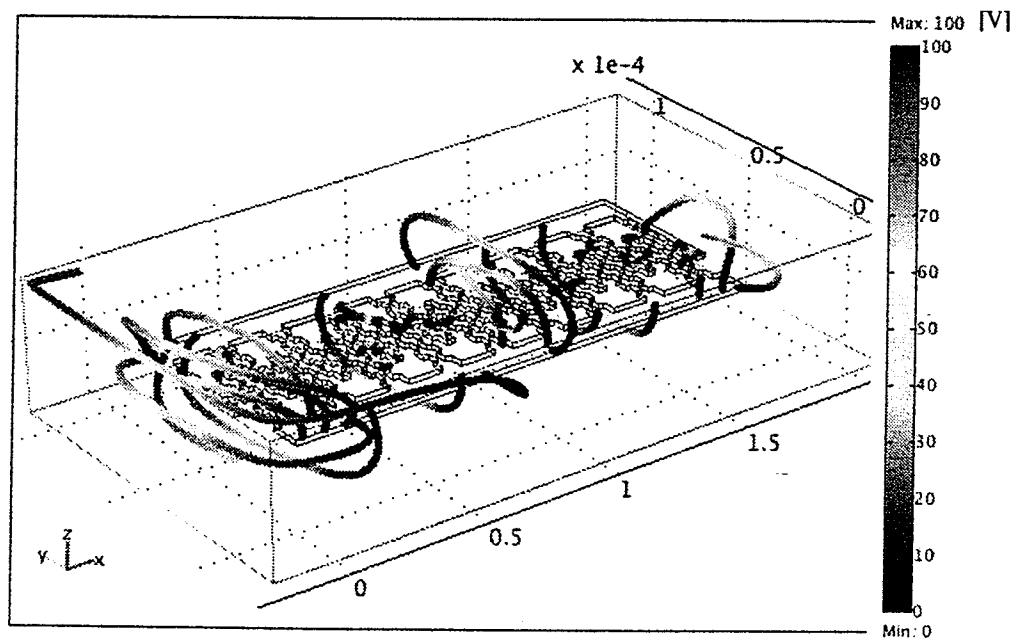


Figure 5.6. Streamlines illustrating the electric field distribution (E). The surrounding volume and device edges follow the electric potential scale 0-100V.

The discrepancies between the 2D- and 3D capacitance analysis were further investigated by a simple model of two parallel, rectangular plates with the same dimensions as the comb fingers. The plates were kept at a constant 3- μm distance from each other. The distance to the edge of the surrounding dielectric volume, i.e. the volume of the 3D integration, was varied as shown in Figure 5.7. Note that the volume of integration directly affects the accuracy of the calculated capacitance due to fringing fields. Since the direct relationship between input voltage and capacitance is expressed as $C = 2W_e/V_0^2$, a quick dimensional examination tells us that, if the 3D capacitance is roughly four times the 2D one, then the required input voltage for 2D simulations should be twice as large as the 3D case.

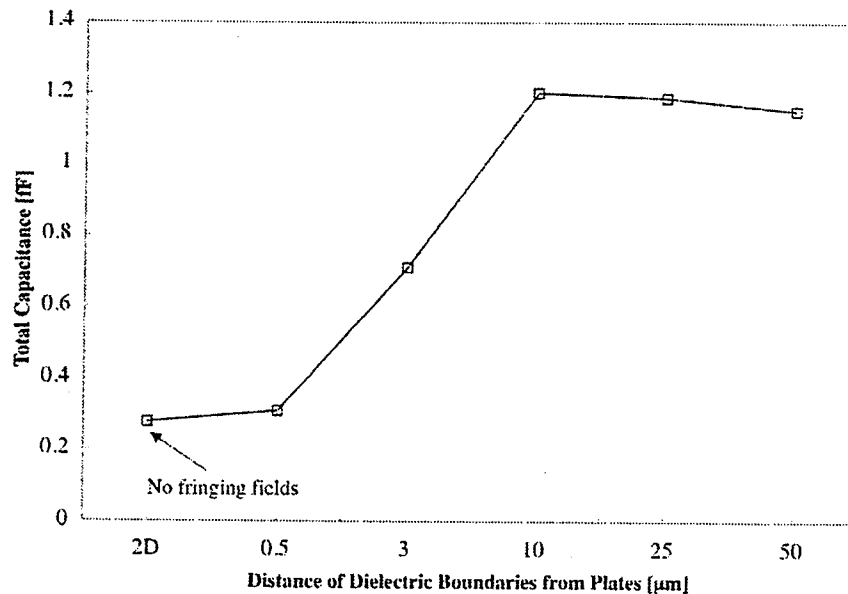


Figure 5.7. Comparison between 2- and 3-dimensional integrations of capacitances. The x-coordinates give the distance between the device boundaries and the surrounding volume boundaries (as described in Figure 5.4)

Furthermore, Figure 5.8 shows that, the presence of a silicon substrate $2\text{ }\mu\text{m}$ underneath the structure affects significantly the value of total capacitance of the structure at any engagement distance. Capacitance is approximately four times larger with the presence of a silicon substrate if compared with the ideal simulation without the substrate. That was in accord with modelling performed in [10], however, the increase in absolute capacitance values alone does not characterize an improvement in the device operation. Figure 5.9 shows the evolution of $\partial C/\partial Y$ with respect to finger displacement. Note that in this plot the “no substrate” case has a more evident rate of change of capacitance than the case in the presence of a substrate. As for the 2D case, since no fringing fields are in plane, the variations in capacitance are less pronounced. Therefore, considering that the concept of step-movement is dependent on $\partial C/\partial Y$, the fact that the total capacitance is larger serves no specific purpose in the move-and-lock mechanism.

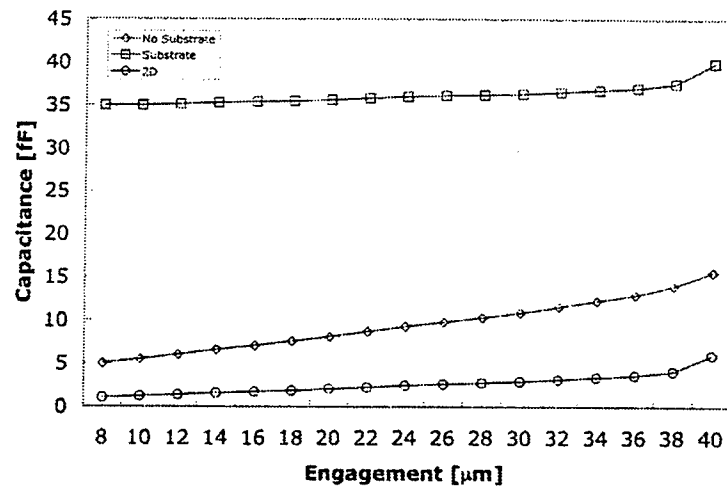


Figure 5.8. These curves represent total capacitance in the jagged-edge model for three different simulation conditions: 3D with Si substrate, 3D without substrate, and 2D.

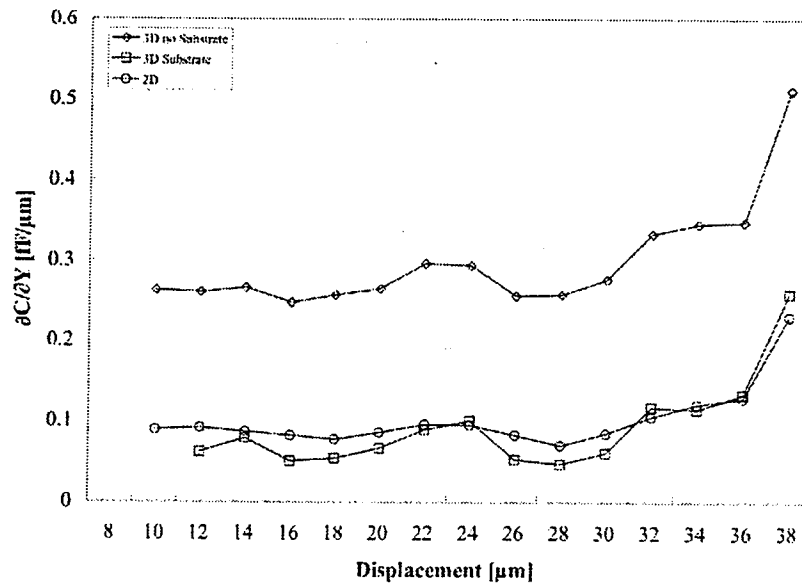


Figure 5.9. Differential capacitance with respect to finger displacement.

5.4 Plane Stress Simulation

Figure 5.10 depicts the spring and its main features. The simulation was carried out with a three-dimensional geometry and tests were run for three different beam lengths. They were 140 μm , 280 μm , and 360 μm long.

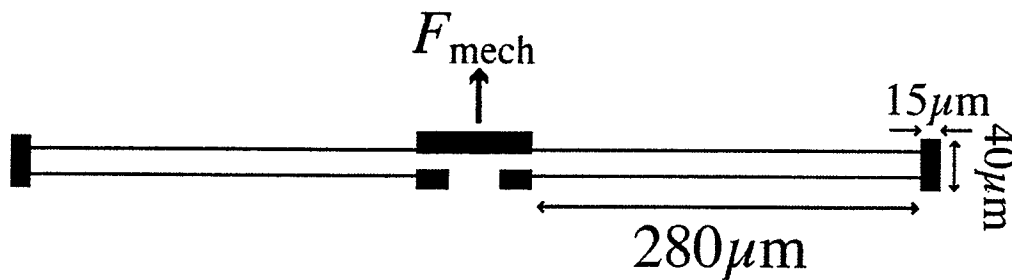


Figure 5.10. Spring design. The spring beam length was simulated for three different lengths: 140-, 280-, and 360- μm .

Non-linear static analyses were performed for several different loads. The loads were applied to the *front wall* of the shuttle (F_{mech}). The loads corresponded to the total electrostatic force (F_{es}) computed in the electrostatic problem at each engagement. The force was then divided by the area of the shuttle front wall and a *force/area* value was computed. The FEM simulation returned continuous values for displacement throughout the spring structure. As expected, the maximum displacement occurred at the shuttle, since both sides of the spring were in equilibrium (Figure 5.11).

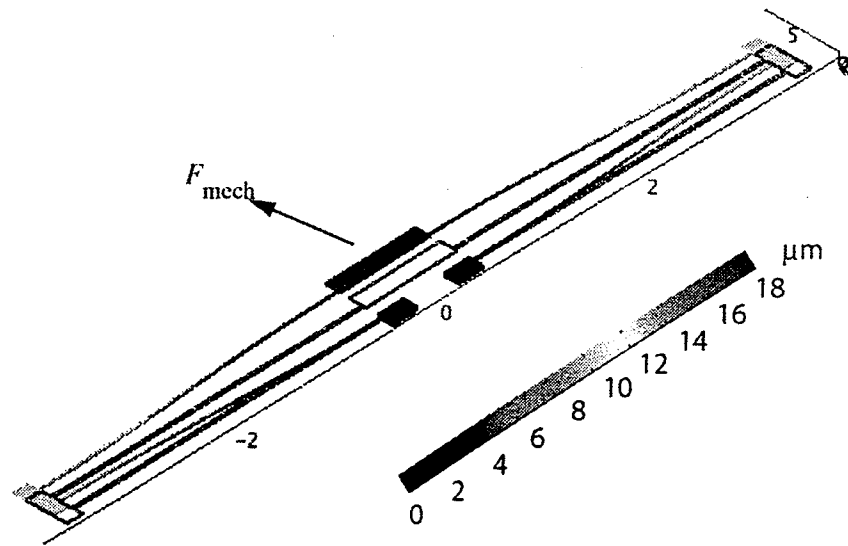


Figure 5.11. Spring displacement due to applied force. F_{mech} is equal in magnitude and direction to F_{es} for a given step movement.

The maximum displacement value for each $F_{mech} = F_{es}$ input was computed as a scalar solution matrix. The spring constant k was computed from $F_{es}/\Delta Y$, where ΔY corresponds to each 2- μm step displacement. Results showed that k was linear for all three simulated springs (Figure 5.12). This plot summarizes what is the necessary force that must be loaded into the system in order to achieve the wanted displacement. Note the significant difference in stiffness between the 140- and 280- μm long springs. Finally, with a known value of k for each of the springs, the spring restoring force was computed for any desired displacement, as further detailed in section 4.5.

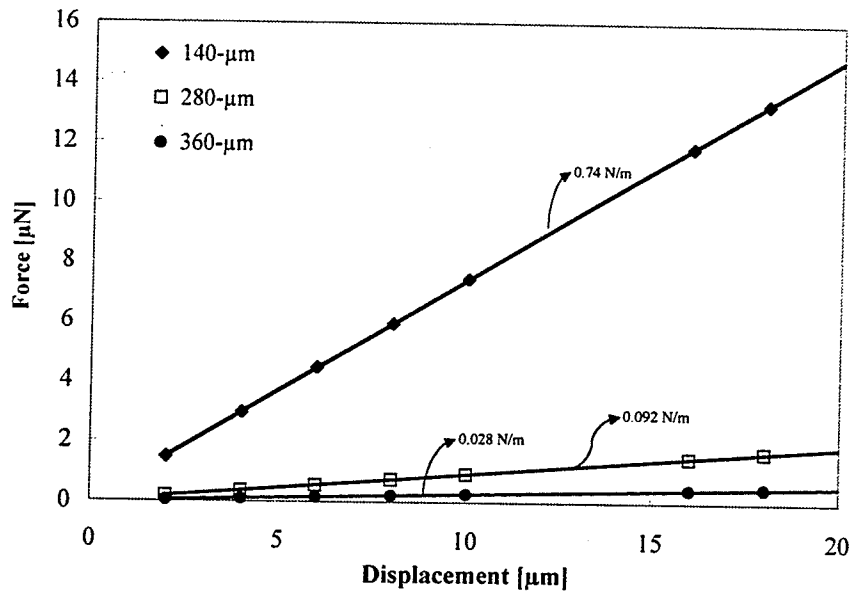


Figure 5.12. Stiffness plot for all three modelled springs with different nominal lengths. The arrows point to each spring constant value.

5.5 Stepped Movement

Figure 5.13 shows the results for combining both the electrostatic and mechanical 3D solutions of the jagged shape comb drive. The operational voltages were arbitrarily chosen not to exceed 100V. The straight lines across the plot show the restoring mechanical force of the 280- μm and 360- μm springs at each engagement step. Hence, the comb drive displacement may be analysed along the spring force line, such that the arrows show *locking points*, where F_{mech} equals F_{es} and the device locks in place. In order to move ahead, higher actuation voltage must be provided to the device. Given that in this experiment the actuation voltage V_0 was chosen to match the 280- μm spring, it is trivial to notice that the 360- μm long spring constant k was characterized as too soft.

Consequently, the use of such spring under the desired V_0 input would not prevent the continuous forward motion of the comb fingers, thus locking would not occur. Conversely, the 140- μm spring was too stiff and produced restoring forces which would require higher electrostatic engaging forces to overcome the spring action (Figure 5.14).

It is important to emphasize that these are arbitrary computations based on a static problem, therefore it is only an approximation and a proof of concept. The simulations described so far do not take into account the interaction between the mechanical and electrostatic domains. The parametric analysis described in Part II delivers a more accurate description of the device performance under conditions similar to the expected operational environment.

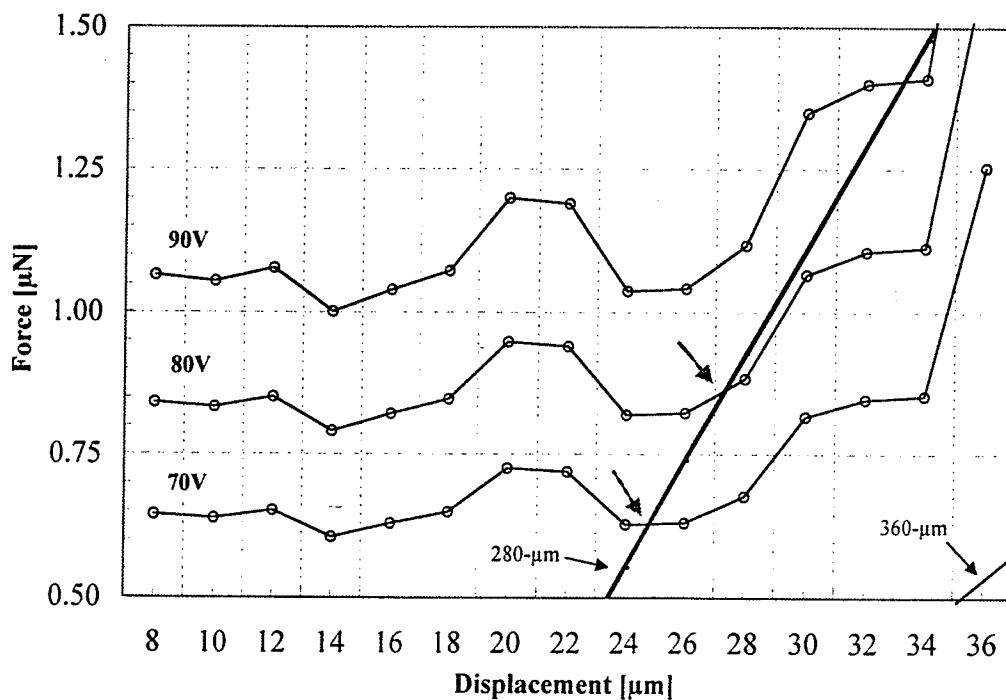


Figure 5.13. Required force for prescribed engagement.

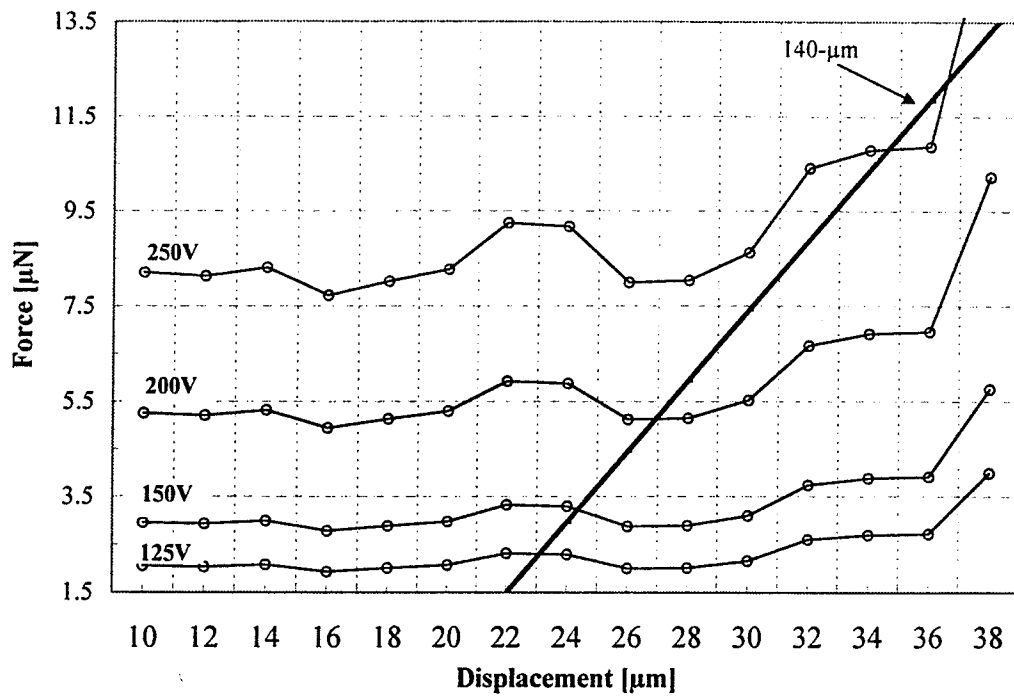


Figure 5.14. Higher actuation voltages are required for implementing the 140-μm spring.

Part II - Electromechanical Multiphysics Solution

So far, the comb drive has been characterized based on independent simulations of the electrostatic and mechanical behaviours of the device. Part II will focus on the coupling of the two problems defined as a *multiphysics simulation*. It is expected that issues regarding the possible non-linear aspects of the design will be properly addressed through multiphysics.

The main challenge in this simulation is the constant change of the electrostatic field as a function of increasing actuation voltage. The parametric character of the simulation comprises an interactive system between the electrostatic *pulling force* and the spring *mechanical restoring force*. The electrostatic equation is solved in the surrounding dielectric (air) domain and resultant forces are the loads of the spring displacement. The present section will deal with the parametric solution of the comb drive operation using the Arbitrary Lagrangian Eulerian method. This model has the spring attached to the comb fingers section of the device at all times, which renders a more realistic simulation.

The ALE simulations presented here were all performed in two dimensions. Although the existence of a substrate below the structure proved to be a relevant parameter, a three-dimensional ALE solution including the ground plane was considered too *costly* in terms of computational time and complexity of the algorithm. A full ALE three-dimensional solution would be beyond the scope of this project. In any case the

reader can have a good estimation of the differences between 2D and 3D results based on the discussion in section 5.3 and the plot in Figure 5.7. The substrate issue and its effect on the total force in this design are further addressed in more detail in the *Future Considerations* section (Chapter 6).

Lastly, it is important to notice that both the electrostatic and the ALE grid displacement computations were based on *weak form* solutions (refer to Appendix II). The mechanical displacement problem was solved by the usual *strong form*, as in Part I. The implementations of the multiphysics problem as well as analysis of the achieved results are discussed below.

5.6 The Comb Drive Analysis with ALE

The simulation of the comb drive problem is characterized by large displacement and small strain with respect to the spring. The electrostatic part of the problem has a time-dependent characteristic, since the voltage load parameter changes in time. However, for the purpose of this thesis all analyses were static for each increment of the independent parameter V_0 (refer to section 3.2.2). The parametric simulation used an array of equally spaced values of V_0 as the independent variable. The expected information from this analysis was twofold: (a) results should reveal the total displacement as a function of input voltage V_0 ; (b) results should emphasize the concept of step movement. Inertial components, such as damping, were not taken into account in this simulation.

It follows that the equilibrium of the system at any iteration point is described by (5-2), where \mathbf{F} and \mathbf{R} are the electrostatic pulling force and mechanical restoring force respectively at a given iteration i . This relation must express the equilibrium of the system for any deformation, considering non-linearities.

$${}^i\mathbf{F} - {}^i\mathbf{R} = \mathbf{0} \quad (5-2)$$

5.7 Formulations and Simulation Set-Up

The ALE simulation developed in this thesis made use of three multiphysics application modes in FEMLAB. Both the electrostatic problem and ALE computational grid displacements were solved with the weak form mode, since no specific ALE module was available in the package. From an operational point of view, the weak mode offered the possibility of building the simulation from scratch, dealing only with PDEs and their respective integral equations. Hence, the user was capable of describing the ALE formulations with a general syntax, which is not as restrictive as other preset physics modes in FEMLAB. The benefits of using the weak form were: (a) for its robustness in dealing with abrupt changes in the scalar field V , defined in the electrostatic problem; and (b) it could adapt to the computational grid domain irregularities easier. Further mathematical descriptions of weak functions and variational form are beyond the scope of this text. Detailed information on this mathematical procedure commonly applied to FEM can be found elsewhere [25].

The ALE grid displacements were defined by Poisson's equation and solved in integral form of the deformed domain.

$$\begin{aligned} \int_{\Omega} \det \mathbf{J} \left[\left(\hat{\delta}x_x I_{xx} + \hat{\delta}x_y I_{yx} \right) \delta x_x + \left(\hat{\delta}x_x I_{xy} + \hat{\delta}x_y I_{yy} \right) \delta x_y \right] d\Omega &= 0 \quad (a) \\ \int_{\Omega} \det \mathbf{J} \left[\left(\hat{\delta}y_x I_{xx} + \hat{\delta}y_y I_{yx} \right) \delta y_x + \left(\hat{\delta}y_x I_{xy} + \hat{\delta}y_y I_{yy} \right) \delta y_y \right] d\Omega &= 0 \quad (b) \end{aligned} \quad (5-3)$$

Where (a) and (b) represent the x - and y -components in the computational grid domain and “ \wedge ” defines a test function. The electrostatic equation starts with Gauss' Law, as shown in (3-2) and transformed into integral form:

$$\varepsilon \int_{\Omega} \det \mathbf{J} \left[\left(\hat{V}_x I_{xx} + \hat{V}_y I_{yx} \right) V_x + \left(\hat{V}_x I_{xy} + \hat{V}_y I_{yy} \right) V_y \right] d\Omega = 0 \quad (5-4)$$

where I_{ij} corresponds to the entries in the inverse Jacobian matrix.

The spring displacement part of the problem used the standard non-linear *plane stress* application mode, available under the *Structural Mechanics module* [54]. The mechanical problem was then solved through the strong form. In this case FEMLAB has the default option of using the PDE that defines Navier's equations (section 3.1.2).

Each application mode had user-defined constraints for boundary conditions, which can be better explained through Figure 5.15a-c. The electrostatic problem is described in 5.15a, where the only constraints are defined in the capacitive structures (fixed and movable set of fingers). The ALE computational grid constraints are described in 5.15b. Note that the grid is free to move in any direction inside the yellow

Chapter 5 Design Simulations and Numerical Solutions

subdomain, which coincides with the dielectric material, i.e., inside the boxed area. The plane stress application mode, depicted in 5.15c has only two constraints. Both of them are anchored boundaries, where no displacement occurs. The constraints defined for the jagged-edge shape comb drive are identical to those defined in the rectangular shape device.

Table 5-1 concisely describes the user interaction with the software tool when setting up the ALE simulation.

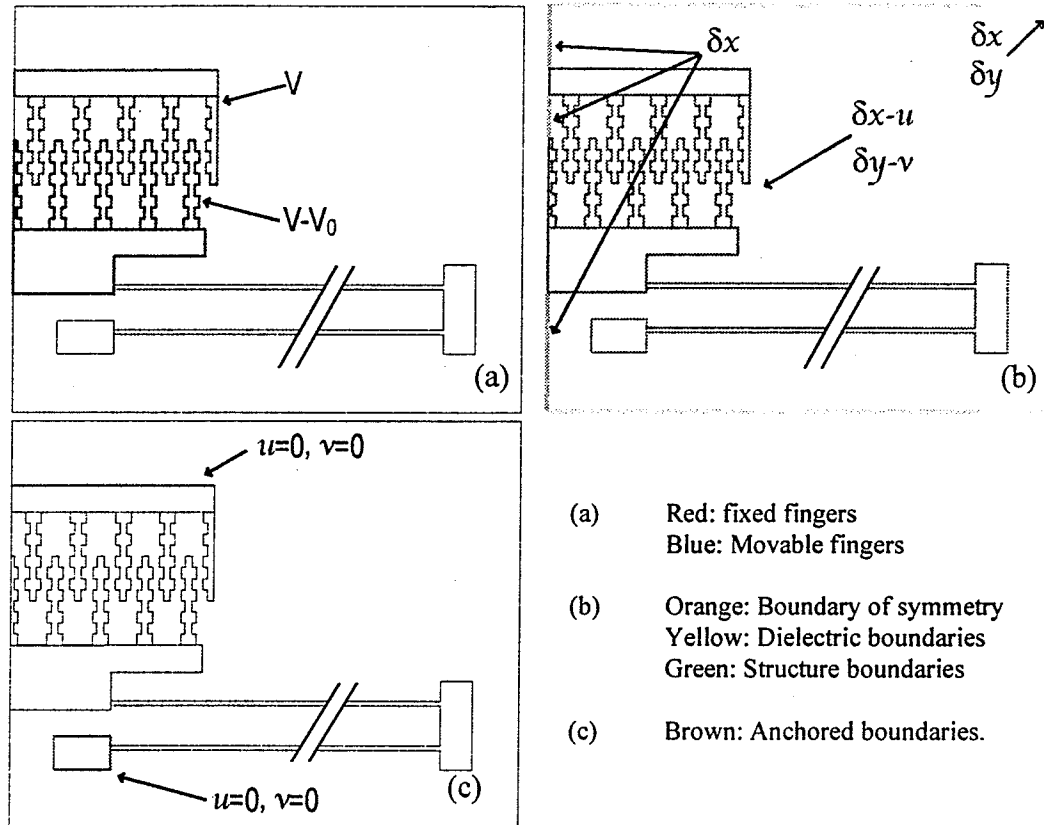


Figure 5.15. Constraints defined in all three multiphysics modes.

Chapter 5 Design Simulations and Numerical Solutions

Table 5-1. Qualitative description of the user-software interaction.

Settings	Description	User Defined	FEMLAB Automatic Set-up (based on user-defined parameters)	FEMLAB Default
<i>General Properties</i>				
Geometry	Shaped Comb Drive	✓		
Constants	Electrostatic and material constants	✓		
Mesh	Type of Element	✓		
	Density			✓
Scalar Expressions	Jacobians, gradients, derivatives	✓		
Equation Systems	Based on Weak Terms and Constraints		✓	
<i>Weak Mode (Electrostatic)</i>				
Subdomain Settings	Weak Term	✓		
Boundary Settings	Weak Term	✓		
	Constraints	✓		
<i>Weak Mode (ALE Grid)</i>				
Subdomain Settings	Weak Term	✓		
Boundary Settings	Weak Term	✓		
	Constraints	✓		
<i>Plane Stress Mode</i>				
Subdomain Settings	Constraints	✓		
	Loads	✓		
Boundary Settings	Constraints	✓		
	Loads	✓		
<i>Solver Settings</i>				
General Settings	Type of Solver			✓
	Parameter	✓		
	Parameter's Values	✓		
Advanced Settings	Number of Iterations	✓		
	Scaling of Variables	✓		
	System Solver			✓

Chapter 5 Design Simulations and Numerical Solutions

According to

Table 5-1 most decisions regarding the simulation set-up procedure are taken by the user. The advantage of choosing a FEA package lies in its ability to automatically set matrix equations based on the parameters entered by the user, as well as offer several options for solver engines.

The implementation of the model, definition of boundary conditions, subdomain settings and material properties can be found in Appendix III. The FEMLAB code is a standard text format, *.m file, which can be reproduced in any computer station where FEMLAB 3.0a or higher is installed. The syntax used to enter equations and arrays is the same used in Matlab, a common engineering and science software widely available.

5.8 Results from the Parametric Analysis

Parametric computations returned the field distribution in the dielectric for input potentials from 0- to 250V. Figure 5.16 depicts consecutive solutions for the parametric simulation of the jagged-edge shape for different input voltages. The comb teeth dimensions are, as previously described in Chapter 4, 40 μ m long with minimum gap distance of 3 μ m and maximum gap of 7 μ m.

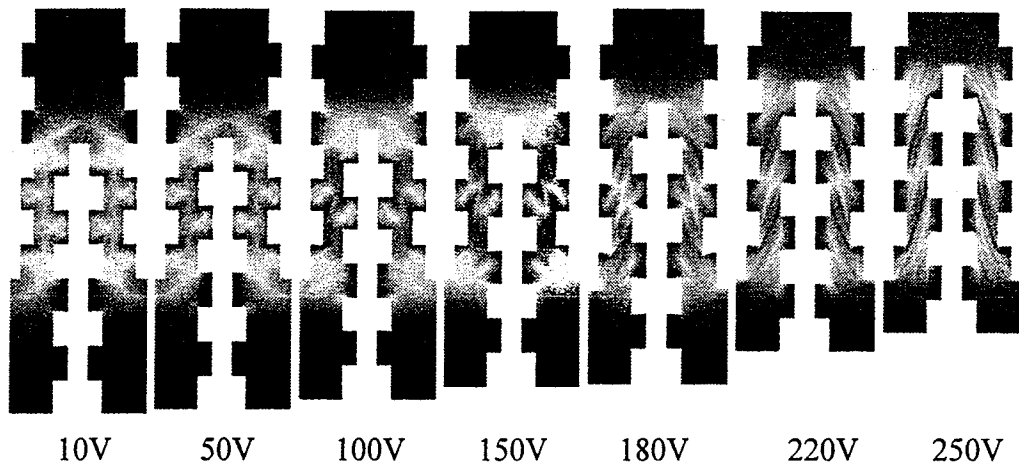


Figure 5.16. Artificial montage depicting the evolution of field lines with increasing voltage.

Next, Figure 5.17a shows electrostatic force results from the same parameters. Forces acting upon the set of movable fingers were computed at each increment of voltage and behaved as a quadratic function of displacement. This response is similar to the one expected from a rectangular shape comb drive with the same dimensions of finger length, thickness and spring length. Figure 5.17b corroborates the information retrieved from the plot in (a), showing the electrostatic force behaviour for a rectangular comb drive with the same dimensions and minimum gap as the jagged-edge structure. The latter is illustrated in Figure 5.18 under the actuation voltage of 200V.

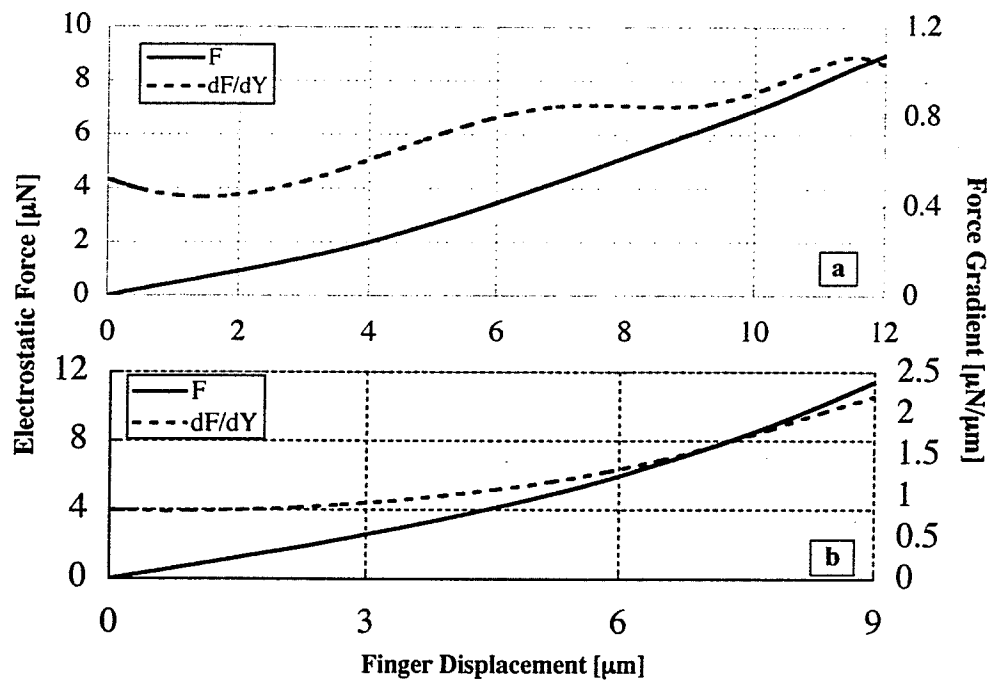


Figure 5.17. Force and force gradient with respect to finger engagement from rest position. Both plots show the force acting on the set of movable (a) jagged-edge fingers and, (b) rectangular fingers.

[m]

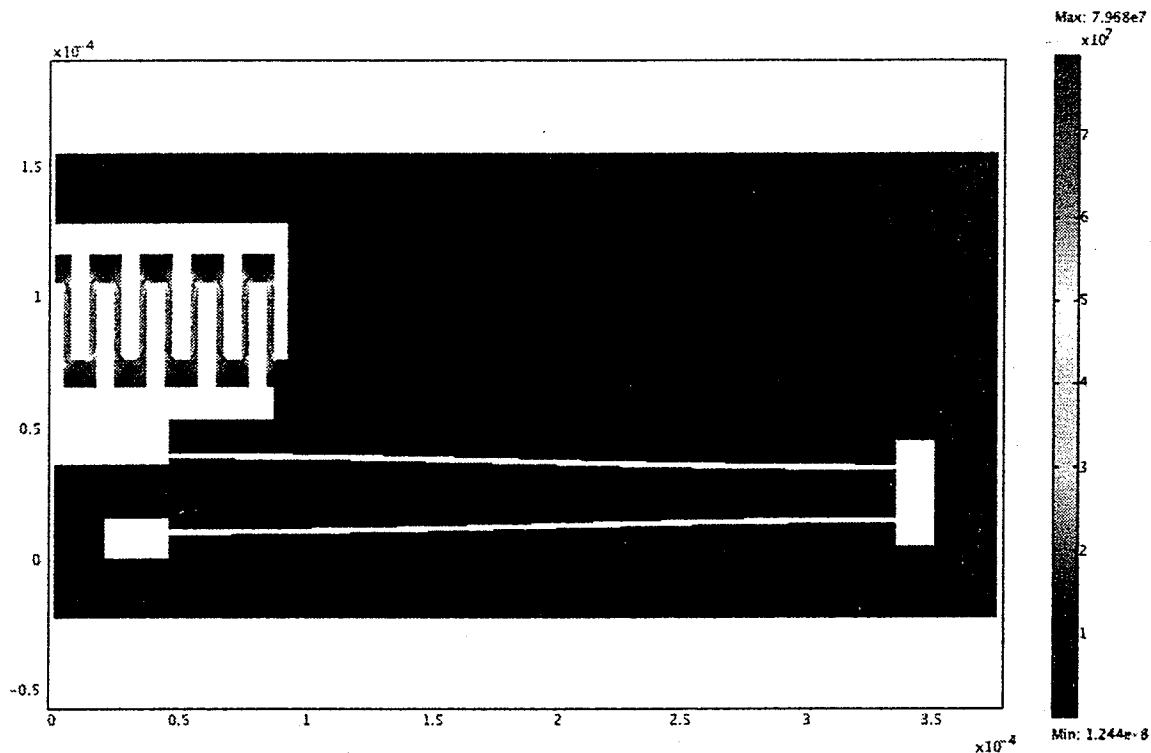


Figure 5.18. FEM solution for the rectangular comb drive. This plot depicts the 200V input parameter.

The comparison between the jagged-edge and rectangular solutions shows a noticeable difference at the force gradient, shown in the secondary axes of Figure 5.17. The jagged-edge shaped produces an evident variable rate of change in force with respect to engagement. The absolute values of the force gradient are however too small, which do not translate into a stepped displacement. This led to the following conclusion: the concept of jagged-edge shape can potentially offer the desired stepped motion, however the dimensions investigated did not yield conclusive results.

As a result of the abovementioned conclusion, new dimensions were investigated, keeping the original concept of jagged-edge comb fingers. The additional shapes

simulated are described in Figure 5.19, which henceforth should be used as a reference to future discussions on jagged-edge shape results.

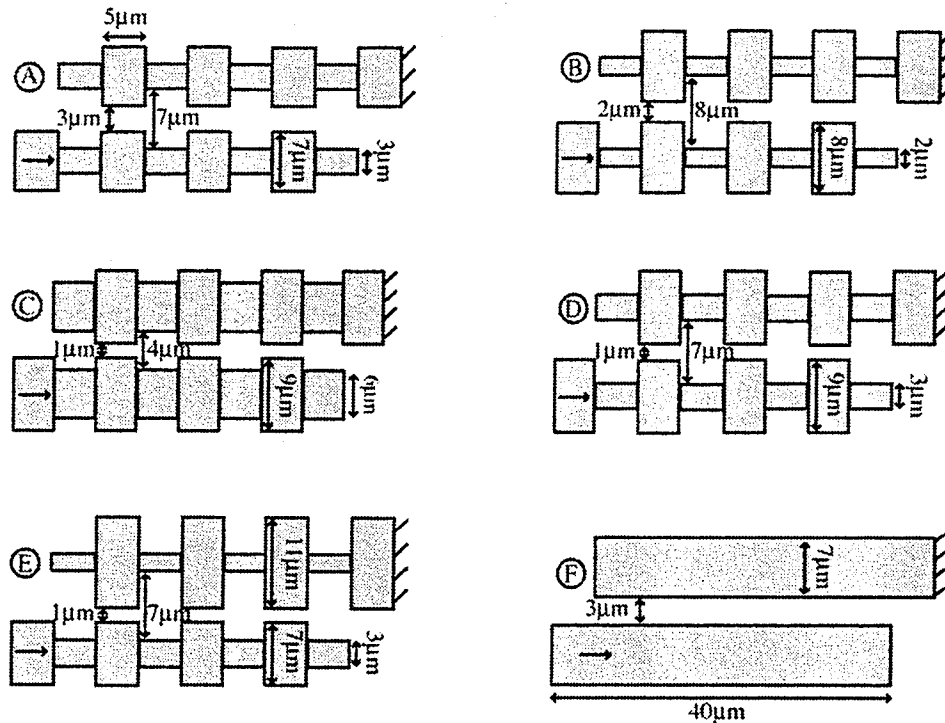


Figure 5.19. Schematic description of: (A) MUMPs design; (B-E) newly proposed jagged-edge finger shapes; (F) rectangular comb finger.

5.8.1 Discussion on Proposed Shapes

The two designs shown in Figure 5.19B and C have 4:1 relationships between maximum and minimum gaps, but with different dimensions. The FEM simulation results (Figure 5.20a) show that the $8:2\mu\text{m}$ gap design has two points of inflection, which are more noticeable than the result for the geometry (A), but still the absolute

displacement values are not enough to justify the design. The 4:1 μm gap design renders an evident step in the total displacement (Figure 5.20b), but the expected “locking positions” shows some minute slippage. This can be seen as the plateaus in the curve for differential displacement with respect to input voltage. The ideal locking position would have zero displacement gradient with respect to the actuation voltage. In Figure 5.21, it can be seen that the force gradient for the 4:1 design shows a change of inflection at 4- μm -displacement from rest position and break points at 6- μm - and 11- μm -displacement. These results show that, at the maximum displacement point of 12 μm from rest position, the 4:1 μm -gap design has the total electrostatic force acting upon the movable fingers about four times larger than those observed in the 8:2 μm gap design.

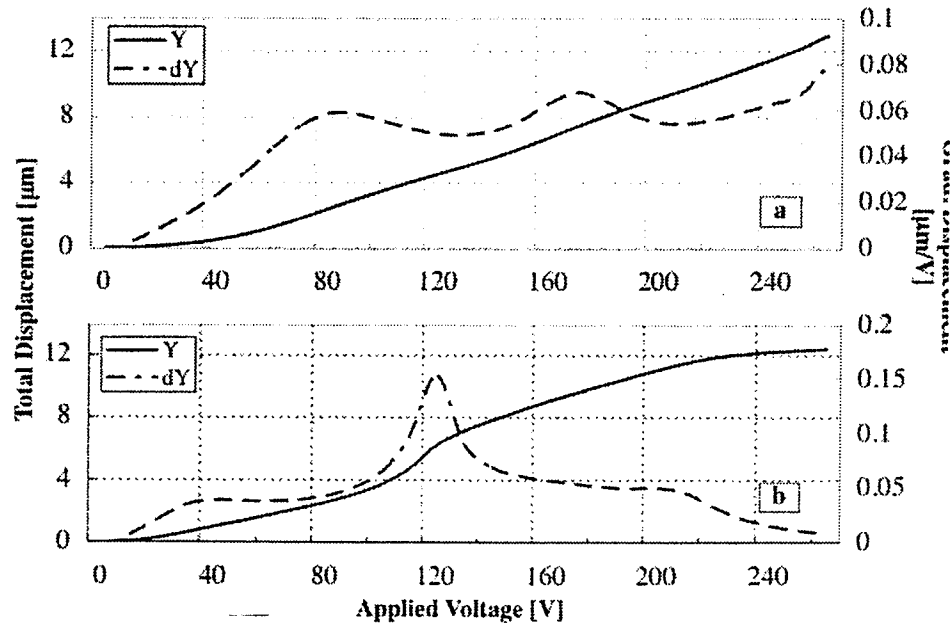


Figure 5.20. Comb displacement with respect to the actuation voltage V_0 . (a) Results from the 8:2 μm -gap; (b) results from the 4:1 μm -gap. The reader should note the difference in scales in the differential displacement axes.

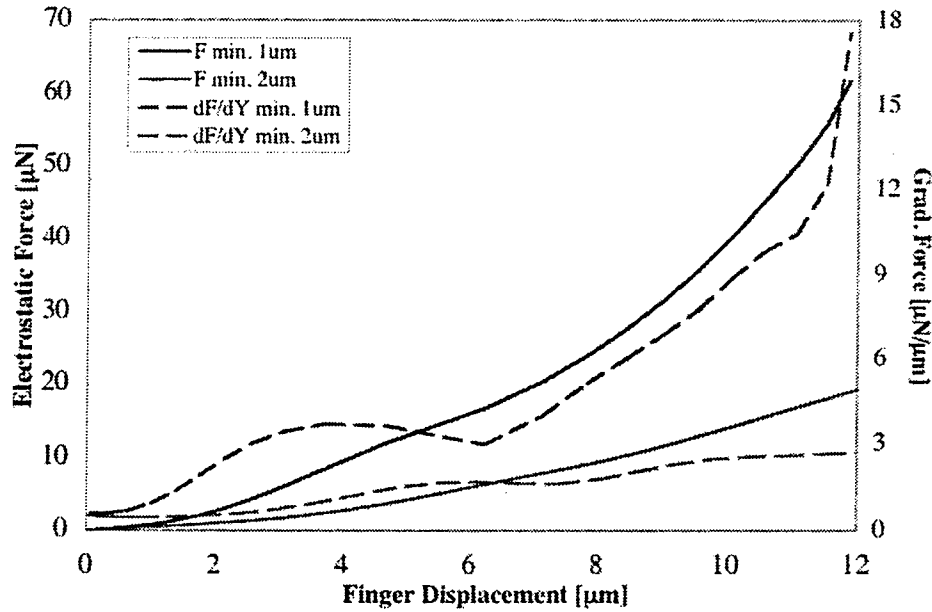


Figure 5.21. Force and force gradient results for both the 4:1μm-gap and 8:2μm-gap designs.

From the above results it is evident that the key factor in the jagged-edge shape design is the ratio between maximum and minimum gaps in conjunction with the actual minimum gap distance value. From these results, the 4:1 ratio with 1-μm minimum gap is more effective than the 4:1 with 2-μm minimum gap. Thus, it is deducible that, for increased gap distances, the dimension of each notch must be increased as well. That is so the gain in notch area balances the increase in gap distance, preserving the total electric energy, as it is described in section 2.1 and synthesized by equation (5-5).

$$W_e = \frac{1}{2} \frac{\epsilon \zeta}{d} V_0^2 \quad (5-5)$$

The designs of Figure 5.19D and E have exaggerated ratios between minimum

and maximum distances with respective values of 1- and 7- μm gaps. Design E, however, is constructed in such a way that the gaps are asymmetric with respect to the imaginary line between the two fingers. The resultant differential displacement with respect to actuation voltage for both these designs is show in Figure 5.22.

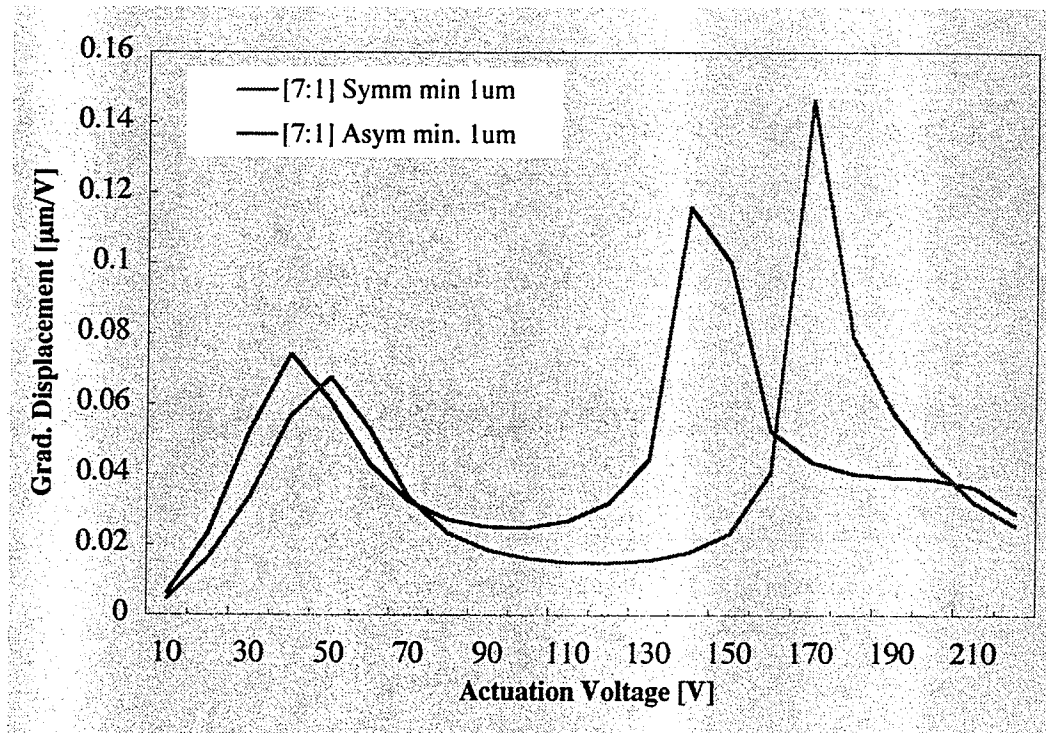


Figure 5.22. Simulated differential displacement with respect to actuation voltage for both symmetric and asymmetric 7:1 designs.

Results for this last analysis are shown in the context of all previous simulations. Figure 5.23 shows combined plots of displacement gradient with respect to actuation voltage. Note that the asymmetric 7:1 design shows two clear points of inflection. The first step in displacement occurs at about 40V. By observing the slope of the curve, it is possible to infer an increase in velocity, which implies that the movable comb finger

accelerates. Given that this is not a dynamic analysis, the lack of inertial components in the system prevents any assumptions with regards to velocities and acceleration under real conditions. In any case, these results show that, under ideal lossless environment, the combined electrostatic-mechanical solution shows a rate of change of displacement with respect to the input parameter V_0 . After 40V the displacement rate as a function of voltage decreases significantly. Ideally, the structure should almost lock in place preventing any Y-direction movement. When the input potential reaches 150V another surge in displacement happens. At this point, the total amount of displacement is larger than in the previous engagement. The general behaviour of the 7:1 symmetric design was similar, but the points of inflection are not as accentuated and the trough not as low, implying more slippage. The following plots illustrate each of the two 7:1 designs in detail. The symmetric design (Figure 5.24) has two engagement steps, but the slippage in the asymmetric design (Figure 5.25) is smaller. It follows that the point of inflection in the force versus displacement plot is more evident in the asymmetric case.

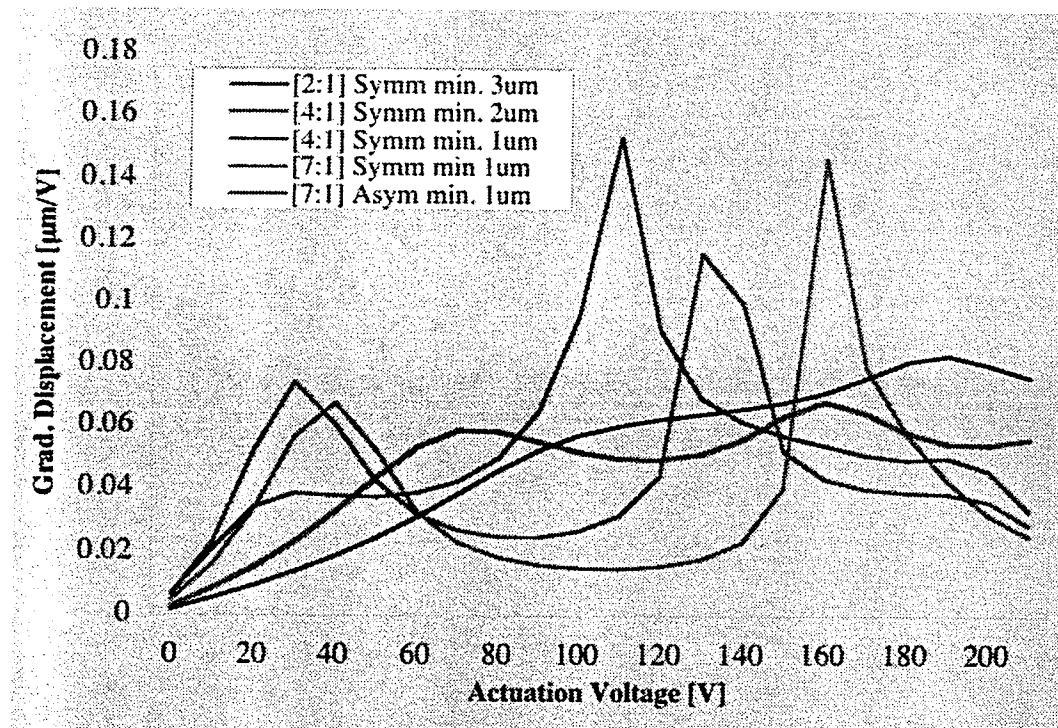


Figure 5.23. Comparison of differential displacements of all geometries investigated.

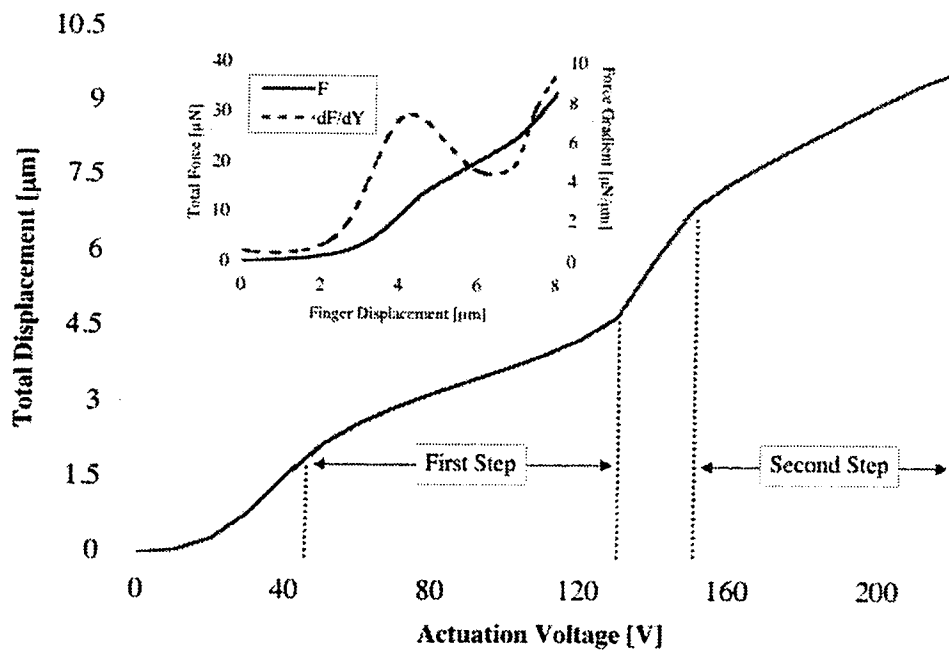


Figure 5.24. Analysis of the 7:1 symmetric design (shape D)

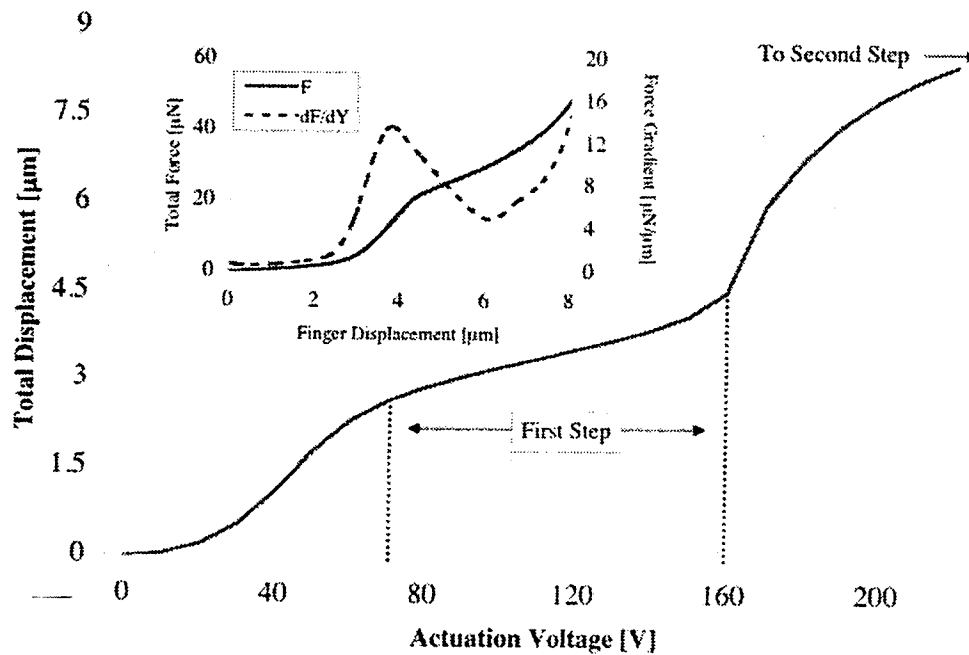


Figure 5.25. Analysis of the 7:1 asymmetric design (shape E).

5.9 Conclusion

The 3D simulations served as an initial proof of the design concept. The use of 3D geometries was justified by the need for proper characterization of the fringing fields effect on total electrostatic force. Independent runs were performed for both the electrostatic and mechanical problems. The solution from the electrostatic simulation served as load to the mechanical model. However, the multidomain nature of the comb drive device required a coupled analysis using a multiphysics model. Due to the complexity of the design, the implementation of a multiphysics simulation in 3D was found to be computationally costly.

The second part of this chapter described a high performance model scheme through ALE formulation. Results illustrated the concept of step movement and showed that, for a given gap ratio and structural thickness, there exists an ideal design correspondent to an asymmetric geometry. Regarding the numerical tools itself, the ALE formulation proved better suited for a multiphysics analysis than the independent static investigations. The use of ALE allows an investigation of the comb drive as a system instead of a composition of individual components. Also, for the purpose of comparison between 2D and 3D results, a fringing analysis was performed.

Chapter 6 Thesis Summary and Future Considerations

6.1 Preamble

This thesis has introduced a novel application to MEMS comb drives operating under DC conditions. The initially proposed designs followed the dimensional requirements of the MUMPs fabrication process. Upon realization, the devices were tested. However, the expected results were not achieved, which promoted a revision of the design principles. Although the general idea remained the same, new dimensions, both in the springs and the comb drive structures were simulated with the finite element method. Satisfactory results were achieved, which proved the viability of the jagged-edge comb drive as an actuator for prescribed force and controlled displacement applications.

6.2 Summary of Investigations

This thesis has introduced a novel application to MEMS comb drives based on an innovative design: the jagged-edge shape comb drive. The intended application of such device is as an actuator to microtweezers, where prescribed forces resulting in controlled displacement are required. Contrary to other MEMS comb drives, this project suggested a device to be operated under DC conditions, removing all lateral oscillation. This design was an improvement to the concept of the sawtooth comb drive, previously introduced in

[6]. The sawtooth comb drive shows sinusoidal behaviour of force versus displacement with a general positive slope as a result of the electrostatic interaction between fixed and movable fingers. Combined with the restoring spring forces, the sawtooth comb drive could potentially show “locking points” where the mechanical spring force balances the electrostatic force. However, the probable locking position corresponds to a single point in the geometry, namely the outer edge of each tooth. This led to the suggestion that, if this locking point was to be extended into a locking area, the device could produce step-movement dependent on the actuation voltage. That is, the jagged-edge shape has a finite plate area for each engaged notch, which produces a stable locking point.

The first part of the investigation dealt with 3D independent electrostatic and mechanical models, describing the comb fingers and cantilever springs respectively. These analyses rendered useful results, as they were enough to validate the concept of stepped-movement. However, the complex interactions between the electrostatic domain as a load to the mechanical domain demanded a more thorough investigation, which could potentially describe the feedback interactions between both domains.

The Arbitrary Lagrangian-Eulerian formulation was chosen as a rigorous tool to combine both domains of interest and produce a multiphysics analysis. Significant effort was put into the implementation of the ALE algorithm as a comb drive modelling procedure. Due to computational cost, this analysis was performed in two dimensions, which, when compared to 3D results, had a scaling factor in the capacitance. Apart from

the lower numerical values for capacitance, the ALE solution was found to be more accurate, since at all instances of the parametric analysis both the electrostatic and mechanical domains of the device are investigated together.

Upon simulating different jagged-edge designs, it was found that the key to achieving the proposed move-and-lock mechanism is optimization of the maximum to minimum gap relationship. Based on the designs investigated, the best result came from an asymmetric 7:1 gap ratio, for a device with 2- μm -thick structural layer.

6.3 Proposed Design Rule

The move-and-lock mechanism is dependent upon two parameters: (a) the rate of change of capacitance with respect to engagement ($\partial C/\partial Y$) and (b) the characteristic spring stiffness. By balancing these two parameters, an optimum solution is possible, which causes the device to move at given voltage intervals and lock with no further displacement. Moreover $\partial C/\partial Y$ can be “adjusted” by scaling the area of each notch in the jagged-edge shape.

This thesis has introduced an initial design rule for jagged-edge comb drives. The designer should start from considering the minimum dimensions possible in the design, given the choice fabrication method. Once the minimum gaps are determined, the relationship between minimum and maximum gaps is established, keeping in mind that

an asymmetric design returns more step-movement instances for a given gap-ratio.

The issue of structural thickness is a balancing factor in this design. If minimum distances are to be increased due to lack of mask resolution or other fabrication limitations, the device thickness can be augmented to match an optimum jagged-edge surface area, which in turn will produce the desired force.

Lastly, the dimension of the springs are also a factor to be considered, albeit not necessarily as a key factor in the design as much as it is a consequence of the desired electrostatic force. Once the maximum electrostatic force for each step is determined, the springs should be designed in such a way that the restoring mechanical force will match the electrostatic force at each desired locking position. Most importantly, this research has shown that the jagged-edge design is greatly adaptable to the designer's requirements, as long as an optimum gap-ratio and thickness relationship is met.

6.4 Future Considerations

Notable points of improvement in the designs presented in this thesis are: (a) optimization of the jagged notch length with respect to structural thickness, which balances the influence of gap distance, and (b) consideration of the slippage problem, which prevents total locking of the device. The present research project can be augmented in two ways:

- Improve numerical models and define an analytical model for the jagged-edge comb drive.

- Develop a fabrication process, which will yield the desired jagged-edge shape with minimum convex edge flattening.

The first point can be achieved by implementing periodic boundary conditions for infinite repetition of the geometry. This would facilitate the development of a *generic simulation*, irrespective of the total number of fixed or movable fingers. Additionally, the simplified implementation would facilitate the use of 3D geometries, which in turn would account for the effects of fringing fields. Moreover, systematic design optimization should be introduced, since the success of this device is dependent upon ideal matching of its dimensions.

As per the increasing the quality of the fabricated device, one option to be considered is the integration of compensating features to sharp edges in the comb fingers. These should prevent smoothing of convex corners. On the other hand, in order to properly fit these compensating features in the lithography mask layout, the total device dimensions should be scaled up. This in turn could raise issues such as sticktion, comb finger bending due to weight and spring buckling. The successful fabrication of the device at ideal dimensions is perceived as the greatest challenge in this project.

Finally, this design could be potentially marketed as long as packaging issues were addressed. The controllable displacement microtweezers could find applications in many different areas of research. Hence, the device must adapt to different packaging requirements, tailored to different applications.

References

- [1] C. Lu, M. A. Lemkin, B. E. Boser, "A monolithic surface micromachined accelerometer with digital output," *IEEE J. Solid-State Circuits*, vol. 30, pp. 1367-1373, 1995.
- [2] E. J. Garcia and J. J. Sniegowski, "Surface micromachined microengine as the driver for micromechanical gears," *Intl. Conf. Solid-State Sensors and Actuators*, Stockholm, Sweden, pp. 365-368, 1995.
- [3] W. C. Tang, T.-C. H. Nguyen, and R. T. Howe, "Laterally driven polysilicon resonant microstructures," in *Tech. Dig. IEEE Micro Electro Mech. Syst. Workshop*, Salt Lake City, UT, pp. 53-59, 1989.
- [4] W. C. Tang, "Electrostatic comb drive for resonant sensor and actuator application," Ph.D. dissertation, Univ. of California, Berkeley, CA, 1990.
- [5] G. T. A. Kovacs, *Micromachined Transducers Sourcebook*, McGraw-Hill, 1998.
- [6] B. J. Jensen, S. Mutlu, S. Miller, K. Kurubayashi, and J. J. Allen, "Shaped comb fingers for tailored electromechanical restoring force," *J. Microelectromech. Syst.*, vol. 12, no. 3, pp. 373-383, 2003.
- [7] D. A. Koester, R. Mahadevan, B. Hardy, and K. W. Markus, *MUMPs Design Handbook - Revision 7.0*, Cronos Integrated Microsystems, Research Triangle Park, NC, USA, 2001.
- [8] T. Mukherjee, Y. Zhou, G. K. Fedder, "Automated optimal synthesis of microaccelerometers," in *Tech. Dig. Twelfth IEEE In. Conf. Micro Electro Mechanical Systems (MEMS'99)*, Orlando, FL, USA, pp. 326-331, 1999.
- [9] W. C. Tang, M. G. Lim, and R. T. Howe, "Electrostatic comb drive levitation and control method," *J. Microelectromech. Syst.*, vol. 1, no. 4, pp. 170-178, 1992.
- [10] W. A. Johnson and L. K. Warne, "Electrophysics of mechanical comb actuators," *J. Microelectromech. Syst.*, vol. 4, no. 1, pp. 49-59, 1995.
- [11] J.-L. A. Yeh, C.-Y. Hui, and N. C. Tien, "Electrostatic model for an asymmetric combedrive," *J. Microelectromech. Syst.*, vol. 9, no. 1, pp. 126-135, 2000.
- [12] W. Ye, S. Mukherjee, and N. C. MacDonald, "Optimal shape design of an electrostatic comb drive in microelectromechanical systems," *J.*

Microelectromech. Syst., vol. 7, no. 1, pp. 16-26, 1998.

- [13] W. Ye, and S. Mukerjee, "Design and fabrication of an electrostatic variable gap comb drive in micro-electro-mechanical systems," *CMES*, vol. 1, no. 1, pp. 111-120, 2000.
- [14] C.-J. Kim, A. P. Pisano, R. S. Muller, and M. G. Lim, "Polysilicon microgripper," *Tech. Dig. IEEE Solid-State and Actuator Workshop*, pp. 48-51, 1990.
- [15] C.-J. Kim, A. P. Pisano, and R. S. Muller, "Silicon-processes overhanging microgripper," *J. Microelectromech. Syst.*, vol. 1, no. 1, pp. 31-36, 1992.
- [16] S. Fetikow and U. Rembold, *Microsystems Technology and Microrobotics*, Springer-Verlag, Berlin, 1997.
- [17] T. Hayashi, "Micro mechanisms," *J. Robotics Mechatronics*, vol. 3, pp. 2-7, 1991.
- [18] G. Greitmann and R. Buser, "Tactile microgripper for automated handling of microparts," *8th Intl. Conf. Solid-State Sensors and Actuators (Euroensors IX)*, Stockholm, Sweden, pp. 372-375
- [19] K.-M. Lee and S. Arjunan, "A three-degrees-of-freedom micromotion in-parallel actuated manipulator," *IEEE Trans. Robotics and Automation*, vol. 7, no.5, pp. 634-641, 1991.
- [20] M Washizu, "Electrostatic manipulation of biological objects in microfabricated systems" in *Integrated Micromotion Systems* ed F. Harashima, Elsevier, pp. 417-31, 1990.
- [21] S. P. Smith, S. R. Bhalotra, A. L. Brody, B. L. Brown, E. K. Boyda, and M. Prentiss, "Inexpensive optical tweezers for undergraduate laboratories," *Am. J. Phys.*, vol. 67, no. 1, pp. 26-35, 1999.
- [22] J. Bechhoefer and S. Wilson, "Faster, cheaper, safer optical tweezers for the undergraduate laboratory," *Am. J. Phys.*, vol. 70, no. 4, pp. 393-400, 2002.
- [23] C. G. Keller and R. T. Howe. "Hexsil tweezers for teleoperated microassembly," *Proc. 10th Annual Intl. Workshop on MEMS (MEMS'97)*, 26-30 Jan. 1997.
- [24] C. S. Pan and W. Hsu. "An electro-thermally and laterally driven polysilicon microactuator," *J. Micromech. Microeng.* vol. 7, pp. 7-13, 1997.
- [25] T. J. R. Hughes, *The Finite Element Method – Linear Static and Dynamic Finite Element Analysis*, Prentice-Hall, New Jersey, 803 pp., 1987.
- [26] V. Adams and A. Askenazi, *Building Better Products with Finite Element Analysis*, Onword Press, Santa Fe, NM, USA, 1999.

- [27] M. Elwenspoek and R. Wiegerink, *Mechanical Microsensors*, Springer-Verlag, Berlin, Germany, 2001.
- [28] Function Reference (meshqual) in *FEMLAB Reference Manual*, COMSOL AB, Stockholm, Sweden, 2003.
- [29] K.-J. Bathe, *Finite Element Procedures in Engineering Analysis*, Prentice-Hall, Englewood Cliffs, NJ, USA, 1982.
- [30] M. S. Gadala, M. R. Movahhedy, and J. Wang, "On the mesh motion for ALE modelling of metal forming processes," *Finite Elements in Analysis and Design*, vol. 38, pp. 435-459, 2002.
- [31] W. Wunderlich, "Incremental formulations for geometrically non-linear problems," in *Chapter 8 - Formulation and Computational Algorithms in Finite Element Analysis: U.S.- Germany Symposium*, ed. K.-J. Bathe, J. T. Oden, and W. Wunderlich, M.I.T. Press, Cambridge, MA, USA pp. 194-240, 1977.
- [32] O. C. Zienkiewicz and R. L. Taylor, *The Finite Element Method, Volume 1: The Basis*, 5th edition, Butterworth Heinemann, Oxford, UK, 689pp., 2000.
- [33] J.-P. Ponthot, "Advances in Arbitrary Eulerian-Lagrangian finite element simulation of large deformation processes," *Fourth Intl. Conf. Computational Plasticity (COMPLAS IV)*, Barcelona, Spain, pp. 2361-2372, 1995.
- [34] J. Wang and M. S. Gadala, "Formulation and survey of ALE method in nonlinear solid mechanics," *Finite Elements in Analysis and Design*, vol. 24, pp. 253-269, 1997.
- [35] P. Vachal, R. V. Garimella, and M. J. Shashkov, "Untangling of 2D meshes in ALE simulations," *J. Computational Phys.*, vol. 196, pp. 627-644, 2004.
- [36] C. W. Hirt, A. A. Amsden, and J. L. Cook, "An arbitrary Lagrangian-Eulerian computing method for all flow speeds," *J. Comp. Phys.*, vol. 14, pp. 227, 1974.
- [37] R. B. Haber, "A mixed Eulerian-Lagrangian displacement model for large deformation analysis in solid mechanics," *Comput. Methods Appl. Mech. Eng.*, vol. 43, pp. 277-292, 1984.
- [38] T. J. R. Hughes, W. K. Liu, and T. K. Zimmerman, "Lagrangian Eulerian finite element formulation for incompressible viscous flows," *Comput. Meth. Appl. Mech. Eng.*, vol. 29, p. 329, 1981.
- [39] M. S. Gadala, "Recent trends in ALE formulation and its applications in solid mechanics," *Comput. Methods Appl. Mech. Engrg.*, in press, 2004.

- [40] *FEMLAB ALE Models Reference Guide*, available from www.comsol.com, 2004.
- [41] A. Beskok and T. C. Warburton, "Arbitrary Lagrangian Eulerian analysis of a bidirectional micro-pump using spectral elements," *Intl. J. Computational Eng. Sci.*, vol. 2, no. 1, pp. 43-57, 2001.
- [42] H. Braess and P. Wriggers, "Arbitrary Lagrangian Eulerian finite element analysis of free surface flow," *Comput. Methods Appl. Mech. Engrg.*, vol. 190, pp. 95-109, 2000.
- [43] J. O. Hallquist, "Simplified Arbitrary Lagrangian-Eulerian" in "LS-DYNA Theoretical Manual – Chapter 14," Livermore Software, 1998.
- [44] A. D. Oliver, D. W. Plummer, "Surface-micromachined mechanisms," Chapter 27 in *The MEMS Handbook*, ed M. Gad-el-Hak, CRC Press, 2002.
- [45] Mechanical Properties of MEMS Materials, Johns Hopkins University, available from: http://titan.me.jhu.edu/~sharpe/Data_Aug16.pdf, 2001.
- [46] Cadence Online Documentation, available from:
http://www.cadence.com/support/education/Cdsdoc_User.pdf, 2003.
- [47] *FEMLAB Reference Manual*, Comsol, AB, <http://www.comsol.com>, 2003.
- [48] J. O. Dow, *Finite Element Methods and Error Analysis Procedures: A Unified Approach*, Academic Press, San Diego, CA, 1999.
- [49] M. Ainsworth, and J. T. Oden, *A Posteriori Error Estimation in Finite Element Analysis*, J. Wiley & Sons, New York, 264 pp., 2000.
- [50] M. Gyimesi, J.-S. Wang, and D. Ostergaard, "Hybrid-element and Trefftz method for capacitance computation," *IEEE Trans. Magnetics*, vol. 37, no. 5, 2001.
- [51] L. Jänicke, and A. Kost, "On the convergence of the finite element method and the reliability of the error estimation," *8th International Symposium on Theoretical Electrical Engineering*, Thessaloniki, Greece, pp. 366-369, 1995.
- [52] B. H. V. Topping, J. Muylle, R. Putanowicz, B. Cheng, and P. Ivanyi, *Finite Element Mesh Generation*, Saxe-Coburg Publications, 250pp., 2004.
- [53] O. Verdier, "Benchmark of Femlab, Fluent and Ansys," *Preprints in Mathematical Science*, 2004:6 LUFTMA-5039-2004, Centre for Mathematical Sciences, Lund University, Lund, Sweden, 2004.
- [54] *FEMLAB 3 Structural Mechanics Module User's Guide*, "Chapter 5 – Continuum Application Modes", Comsol, AB, Stockholm, Sweden, 2004.

Appendix I The Principle of Virtual Work

The Principle of Virtual Work (PVW) is a common numerical technique applied in structural mechanics and electrostatics. Let *virtual displacement* be an infinitesimal change in the geometry of a system as the result of the forces and constraints imposed on the system at a given time. The PVW states that a system of real forces is in equilibrium if and only if the virtual work performed by these forces is zero for all virtual displacements that are compatible with geometrical boundary conditions.

Recall that a capacitor is characterized by two parallel plates separated by a dielectric layer, where one plate has positive and the other negative charges. Hence, an attractive electrostatic force exists between the plates. This force is calculated based on the charge distribution on the capacitor plates. Figure A-I.1 demonstrates the virtual displacement of a comb finger. In the context of this thesis, FEM simulations are used to calculate the electrostatic field energy present in the system; which in turn is integrated over the structure's surrounding volume, returning the total capacitance in the system at a given finger engagement.

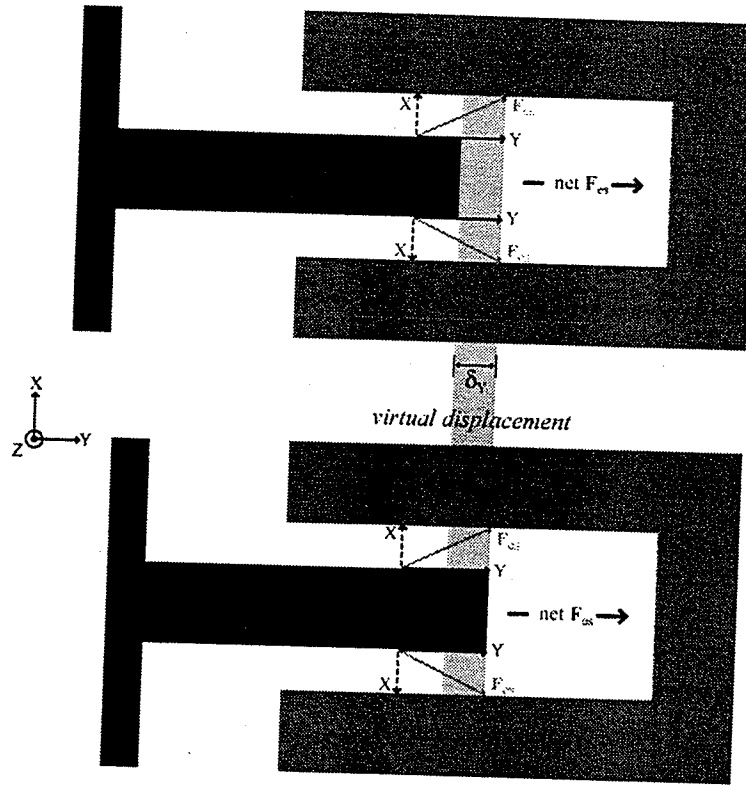


Figure A-I.1. Schematic description of the virtual displacement. The X-components of the electrostatic force F_{es} are cancelled by the opposite vector. The Y-components are added together.

The electrostatic force acting upon the movable finger is obtained by assuming a differential displacement of the body in the Y-direction (δ_y) and computing the resulting change in the electrostatic energy of the system. The PVW is dependent upon the assumption the comb fingers maintain a constant voltage. The energy W_e changes as the geometry (and hence C) changes. The stored electrical energy of such a system is:

$$W_e(\bar{Y}) = \frac{1}{2} C(\bar{Y}) V^2 = \frac{1}{2} C V^2 \delta_y \quad (\text{A-I.1})$$

In order to move the capacitors plates, work is necessary. This work is caused by the force F_{es} that the plates of the capacitor exert on each other, as seen in below:

$$F_{es} = \nabla W_e = \frac{\partial W_e(Y)}{\partial Y} = \frac{CV^2}{2d} \delta_Y \quad (A-I.2)$$

As described in Figure A-I.1, if C depends on a single dimension Y , the magnitude of the force between the fingers is dependent on the rate at which work is done per unit Y -displacement. Note that, for the purpose of the PVW analysis, the X -components of the electrostatic force F_e are cancelled by the opposite vector. The Y -components are added together.

Additional Readings

1. D. DaDeppo, *Introduction to Structural Mechanics and Analysis*, Prentice Hall, 480pp., 1998.
2. B. F. Romanowicz, *Methodology for the Modelling and Simulation of Microsystems*, Kluwer Academic Publishers, 136pp., 1998.

Appendix II Theoretical Principles of FEM

A-II.1 Introduction

The finite element method is based on the fundamental concept that a given continuous function defining a structured geometry can be approximated by a *discrete model*. The approximation is done by subdividing the geometry into a finite number of elements, hence the name *finite element method*. Figure A-II.1 shows a hierarchical description of a three dimensional element and its characterizing features. The terminology is the same for both two- and three-dimensional models and Figure A-II.1 should serve as reference throughout this text.

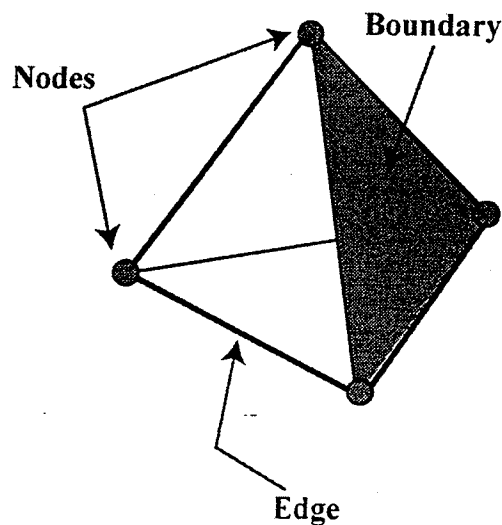


Figure A-II.1. Description of a three-dimensional element and its respective features.

(a) NODES: Points where unknown functions (variables of interest) are calculated. To each node, correspond a number of unknown functions, which are the *degrees of freedom* (DOF) at that node.

(b) EDGES: The edges are defined by *interpolation functions* or *polynomials*, which describe the behaviour of the variable of interest between the nodes. The edges can be subdivided by *midpoints*, which define higher order polynomials. Higher order elements offer a better approximation of the original geometry.

(c) BOUNDARIES: Mathematically classified according to the behaviour of the unknown variable inside the boundary domain. The *Dirichlet condition* specifies the numerical value of the unknown at the boundary, whereas the *Neumann condition* defines the first derivative of the unknown normal to the surface.

(d) SHAPE FUNCTIONS: The coefficient that qualifies the interpolation polynomial. Each node has a corresponding shape function defined in terms of independent variables, such as the coordinate system X, Y, Z . The function returns the magnitude value of 1 at its defining node and 0 at all other nodes.

The concepts introduced above can be further explained for the case of a single arbitrary, one-dimensional variable w , defined in equation (3-13). The variable w can be approximated with a function described by a finite number of parameters or DOFs at each node w_i , where φ are the shape functions.

$$w(x) = W_1\varphi_1(x) + W_2\varphi_2(x) + W_3\varphi_3(x) + \cdots + W_n\varphi_n(x) \quad (\text{A-II-1})$$

The FE analysis delivers an approximate solution, which is only *as accurate as* the quality of the mesh approximation, the material properties used and their assumptions, and the definition of the loads and boundary conditions. The solution algorithm is also a source of potential inaccuracies and must be chosen based on proper assessment of the physical problem.

A-II.1.1 Mesh Generation

The basis of the FEA is the development of a good quality approximation of the geometry under scrutiny. For that reason the mesh generation is a fundamental step in achieving meaningful results. The discretization of the model is achieved through the creation of a mesh of elements, which approximate the geometry. The mesh *density* is defined as the number of elements per unit area for a two-dimensional model and elements per unit volume for the three-dimensional case. The quality of the approximation depends upon the quality q of each element according to (A-II-2a-b) for 2- and 3-D cases. The side length of the triangular element is represented by h_i , whereas area and volume are a and V respectively [28].

$$\left\{ \begin{array}{ll} q = \frac{4a\sqrt{3}}{h_1^2 + h_2^2 + h_3^2} & (\text{a}) \\ q = \frac{216}{\sqrt{3}} \frac{V}{(h_1^2 + h_2^2 + h_3^2 + h_4^2 + h_5^2 + h_6^2)^{3/2}} & (\text{b}) \end{array} \right. \quad (\text{A-II-2})$$

The element quality is directly related to its geometry. Elements with similar edge sizes will return higher quality values than those with uneven shapes, which in turn will influence the final convergence of the model solution. Figure A-II.2 illustrates the idea of element quality related to the element dimensions in 2D; the same concept applies to 3-dimensional elements.

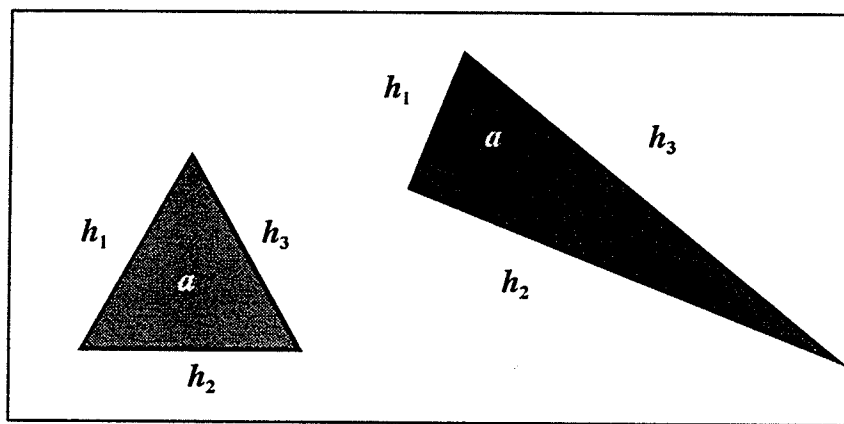


Figure A-II.2. Schematic description of a higher quality element (red), and a lower quality element. The sides are h_i and the element area is a .

A-II.1.2 Types of Element

Each element in an FE mesh is characterized by predefined numerical formulations. Common problems involving large structure deformation and fluid mechanics use mainly two types of formulation: the *Lagrangian element* and the *Eulerian element* [29].

In the case of the Lagrangian formulation, the FE mesh is attached to the structure under analysis and it follows the motion of the body from the original to the final configuration of the body geometry. This approach is popular in solid mechanics,

especially in cases where unconstrained flow occurs over free boundaries [30]. That is because the mesh closely approximates the structure boundaries. The disadvantage of this formulation is its poor solution convergence in problems such as: large deformation, nonlinear boundary conditions, boundary conditions which vary as different loads are applied, or when meshes element distortion is excessive.

The Eulerian formulation utilizes a mesh fixed in space while the analysed structure flows through the mesh. The fixed mesh represents a *control volume* [31] that is static, if seen from the point of view of the moving structure. It follows that, since the mesh is spatially fixed, no mesh distortion occurs. On the other hand, the Eulerian formulation is not a suitable approach for structural problems where large displacement occurs. For the reason that at each instance where the structure moves beyond the boundaries of the control volume, a new volume would have to be created. Additionally, in the cases where the analysed structure flows without constraints through free boundaries, this approach is unable to return a solution, unless the boundaries of the deformed structure are known in advance. Nonetheless, this is a robust approach for fluid mechanics problems enclosed in a fixed volume, i.e. large material flow, but minimal change in boundary shape.

When the comb drive problem is considered, three issues must be taken into account before determining the appropriate element to be used in the analysis. They are: (a) spring displacements are large with respect to the spring dimensions; (b) as long as

arching does not occur between the movable and fixed fingers, the comb drive lateral displacement is unconstrained; (c) due to (b), the boundary conditions of this problem do not remain constant during the change of loads as a function of voltage increments. These statements imply that neither Lagrangian nor Eulerian formulations alone would return successful solutions for the comb drive simulation. One could argue that, the advantages of each method are the weakness of the other, and the two methods complement each other in this respect [30]. The next section will discuss an alternative approach to deal with large deformation problems, which couples both mesh elements discussed in this section.

A-II.1.3 Formulations

As previously described, FEM models are discrete; hence, all functions must be approximated by a finite number of elements. Given an unknown, multidimensional and continuous function $\mathbf{w}(x,y,z)$ defined in the domain Ω , the objective of the analysis is to describe \mathbf{w} such that it satisfies a set of partial differential equations $\Theta(\mathbf{w})$, where Θ is an operator, as in equation (A-II-3). The PDE description of a problem is also referred to as the *strong formulation*.

$$\Theta(\mathbf{w}) = \begin{Bmatrix} \Theta_1(\mathbf{w}) \\ \Theta_2(\mathbf{w}) \\ \vdots \end{Bmatrix} = 0 \quad (\text{A-II-3})$$

Each element in the FEM mesh has a set of appropriate boundary conditions $\mathbf{B}(\mathbf{w})$

defined in the domain Ω .

$$\mathbf{B}(\mathbf{w}) = \begin{Bmatrix} B_1(\mathbf{w}) \\ B_2(\mathbf{w}) \\ \vdots \end{Bmatrix} = \mathbf{0} \quad (\text{A-II-4})$$

Equations (A-II-3) and (A-II-4) are solved by the introduction of a set of functions \mathbf{v} , which are equal in number to the components of \mathbf{w} .

Then the equations in (A-II-4) can be superimposed to reconstitute the domain Ω , as shown in (A-II-5):

$$\int_{\Omega} \mathbf{v}^T \boldsymbol{\Theta}(\mathbf{w}) d\Omega \equiv \int_{\Omega} [v_1 \Theta_1(\mathbf{w}) + v_2 \Theta_2(\mathbf{w}) + \dots] d\Omega \equiv 0 \quad (\text{A-II-5})$$

The statements so far have shown that the FEM problem, when integrated, returns a solution to the continuous problem. It must be noted that the boundary conditions imposed by (A-II-4) are to be simultaneously satisfied in order to obtain a convergent solution, where \mathbf{u} is a set of arbitrary functions:

$$\int_{\Gamma} \mathbf{u}^T \mathbf{B}(\mathbf{w}) d\Omega \equiv \int_{\Gamma} [u_1 B_1(\mathbf{w}) + u_2 B_2(\mathbf{w}) + \dots] d\Omega \equiv 0 \quad (\text{A-II-6})$$

In summary, the integral statement seen in equation (A-II-7) recovers the same solutions sought with the PDEs described by equations (A-II-3) and (A-II-4) combined.

$$\int_{\Omega} \mathbf{v}^T \boldsymbol{\Theta}(\mathbf{w}) d\Omega + \int_{\Gamma} \bar{\mathbf{v}}^T \mathbf{B}(\mathbf{w}) d\Omega = 0 \quad (\text{A-II-7})$$

If the operator $\boldsymbol{\Theta}$ has a higher order of differentiation than that "acceptable" by \mathbf{w} , then the derivative function is discontinuous and the expression in (A-II-7) is *non-square*

integrable. Recall that a function of a real variable is considered square-integrable on a given domain if the integral over that domain of the square of its absolute value is finite, such that $\int_{-\infty}^{\infty} |f(w)|^2 dw$.

A general way to solve this issue, is by introducing the *weak form* of the problem. The idea of the weak form is to provide a more “lenient” statement of the problem, which can “adapt” to the discontinuities of the function w . That is achieved by performing integration by parts on (A-II-7) and replacing it by (A-II-8).

$$\int_{\Omega} \mathbf{C}(\mathbf{v})^T \mathbf{D}(\mathbf{w}) d\Omega + \int_{\Gamma} \mathbf{E}(\mathbf{u})^T \mathbf{F}(\mathbf{w}) d\Omega = 0 \quad (\text{A-II-8})$$

In this case, the operator \mathbf{C} , \mathbf{D} , \mathbf{E} , and \mathbf{F} have lower order derivatives than the corresponding ones in equation (A-II-7).

The derivation of the weak form is widely described in FEM literature; the reader is encourage to look for more information in [25], [29], [32]. Additionally, the software package used in this thesis (FEMLAB) offers a *weak form mode*, where the user has to enter the appropriate integrands, but the weak transformations and test functions are automatically generated by the package.

Appendix III FEMLAB Code

This appendix shows an example of an analysis file generated in FEMLAB 3.0a. The code uses common Matlab syntax and can be reproduced either as *.m file or saved as a native FEMLAB file *.fl.

```
% FEMLAB Model M-file
% Generated by FEMLAB 3.1 (FEMLAB 3.1.0.157, $Date: 2004/11/12 07:39:54 $)
% Some geometry objects are stored in a separate file.
% The name of this file is given by the variable 'flbinaryfile'.

flclear fem

% Femlab version
clear vrsn
vrsn.name = 'FEMLAB 3.1';
vrsn.ext = '';
vrsn.major = 0;
vrsn.build = 157;
vrsn.rcs = '$Name: $';
vrsn.date = '$Date: 2004/11/12 07:39:54 $';
fem.version = vrsn;

flbinaryfile='jagg_sym_1g7.flm';

% Constants
fem.const={'epsilon','8.854e-12','V0','1600'};

% Geometry
clear draw
g22=flbinary('g22','draw',flbinaryfile);
g641=flbinary('g641','draw',flbinaryfile);
g10=flbinary('g10','draw',flbinaryfile);
g9=flbinary('g9','draw',flbinaryfile);
g13=flbinary('g13','draw',flbinaryfile);
draw.s.objs = {g22,g641,g10,g9,g13};
draw.s.name = {'CO1','CO5','CO6','CO3','CO2'};
draw.s.tags = {'g22','g641','g10','g9','g13'};
fem.draw = draw;
fem.geom = geomcsg(fem);
```



```

matl.alpha = '4.15e-6';
matl.E = '158e9';
lib.matl = matl;
fem.lib = lib;

% Multiphysics
fem=multiphysics(fem);

% Extend mesh
fem.xmesh=mesextend(fem);

% Solve problem
fem.sol=femnlin(fem, ...
    'nullfun','fnullorth', ...
    'solcomp',{'lm7','dx','u','dy','lm8','V','v'}, ...
    'outcomp',{'lm7','dx','u','dy','lm8','V','v'}, ...
    'pname','V0', ...
    'plist',[0:10:220]));

% Save current fem structure for restart purposes
fem0=fem;

% Plot solution
postplot(fem, ...
    'tridata',{'absVx_es','cont','internal'}, ...
    'trimap','jet(1024)', ...
    'deformsub',{'dx','dy'}, ...
    'deformscale',1, ...
    'solnum',3, ...
    'title','V0(3)=20 Surface: |grad(V)| Displacement: dx,dy', ...
    'refine',1, ...
    'geom','off', ...
    'axis',[-1.87500001629815E-5,3.9375000342261E-4,-5.65357136760472E-
5,1.84535716990857E-4,-1,1]);

```